



Rational modulation of Fe single-atom electronic structure in a Fe-N₂B₄ configuration for preferential ¹O₂ generation in Fenton-like reactions

Yuhan Long^a, Zhenhua Cao^a, Weiran Wu^a, Wenhao Liu^a, Peizhen Yang^b, Xuesong Zhan^c, Rongzhi Chen^d, Dongfang Liu^{a,*}, Wenli Huang^{a,*}

^a Tianjin Key Laboratory of Environmental Technology for Complex Trans-Media Pollution, College of Environmental Science and Engineering, Nankai University, Tianjin 300350, China

^b School of Environment, Tsinghua University, Beijing 100084, China

^c National & Local Joint Engineering Research Center on Biomass Resource Utilization, College of Environmental Science and Engineering, Nankai University, Tianjin 300350, China

^d Yanshan Earth Critical Zone and Surface Fluxes Research Station, College of Resources and Environment, University of Chinese Academy of Sciences, Beijing 100049, China

ARTICLE INFO

Keywords:

Single-atom catalysts
Singlet oxygen
Fenton-like reactions
Electronic structure modulation
Peroxymonosulfate

ABSTRACT

The important role of optimizing the coordination environment of single-atom catalysts (SACs) for selective production of singlet oxygen (¹O₂) in Fenton-like reactions is revealed. Herein, we introduce electron-depletion boron atoms to manipulate the coordination number and atom types of Fe site simultaneously and construct a six-coordination Fe-N₂B₄ catalyst for peroxymonosulfate (PMS) activation. Particularly, it achieves 98.68% ¹O₂ generation selectivity superior to unregulated Fe-N₄ catalyst (64.57%), exhibiting an exceptional bisphenol A (BPA) degradation performance with a reaction rate constant of 0.249 min⁻¹. Experimental and theoretical results unveil that the tailored electronic structure of Fe not only enhances the adsorption selectivity of terminal oxygen atoms in PMS and alters the reaction pathway preference, but also facilitates the electron donation from PMS and lowers the energy barrier for ¹O₂ generation. This work provides a universal strategy for rational and precise modulation of SACs for specific reactive species conversion in environment remediation.

1. Introduction

With the speedy evolution of society, the widespread use of chemicals inevitably resulted in the increasing concentration of persistent organic pollutants in the water bodies, which is difficult to eliminate by conventional water purification techniques [1]. Recently, advanced oxidation processes (AOPs), as promising green decontamination technology, demonstrated enormous potential for aqueous pollutant remediation using strong oxidative radicals generated in situ [2,3]. Among these, peroxymonosulfate (PMS)-based Fenton-like reactions have drawn extensive attention for the rapid elimination of resistant organic contaminants due to the highly generated reactive oxygen species (ROS) such as sulfate radical (SO₄^{•-}), hydroxyl radical (•OH), superoxide radical (O₂^{•-}), high-valent metal species and singlet oxygen (¹O₂) [4–6]. However, the existing complicated pollutants with miscellaneous toxicity and multiple anions in wastewater hinder the PMS activation and decontamination efficiency by various reactive species, restricting the

utilization of Fenton-like reactions significantly [7]. Compared to other ROS, ¹O₂ is considerably more universal due to its high affinity to electron-rich organic contaminants, remarkable versatility in inorganic ion resistance, and long life for persistent oxidation [8,9]. Many transition metal (Co, Fe, Cu) based and carbon-derived materials have proved to be effective PMS activators toward ¹O₂ production [10–12]. At present, there are two main pathways involved in ¹O₂ generation: (i) PMS acts as an electron acceptor. In this process, the generation of ¹O₂ is commonly accompanied by various radicals after cleavage of O–O bond in PMS, restricting its practical application in complex water restoration; (ii) PMS acts as an electron donor. ¹O₂ was mainly generated via SO₅^{•-} self-decomposition after PMS adsorption on the catalyst surface [9]. Given that, the development of innovative techniques to regulate the activation pathway of PMS and enhance the yield of potent reactive ¹O₂ is immensely desired.

Single-atom catalysts (SACs), which contain atomically distributed metal sites embedded on the support, were developed recently for highly

* Corresponding authors.

E-mail addresses: dongfangli@nankai.edu.cn (D. Liu), huangwenli@nankai.edu.cn (W. Huang).

<https://doi.org/10.1016/j.apcatb.2023.123643>

Received 12 October 2023; Received in revised form 14 December 2023; Accepted 17 December 2023

Available online 21 December 2023

0926-3373/© 2023 Published by Elsevier B.V.

utilizing active sites to improve catalytic performance, selectivity, and long-term reliability in Fenton-like reactions [13–15]. Presently, the commonly-reported SACs rely on M-N₄ (M = Fe, Cu, Co, Mn, etc.) configuration with four M-N bonds on a single dimension, performing as efficient Fenton-like catalysts in the organic compound elimination [2, 16], especially for ¹O₂ selective generation. For instance, Mi et al. developed the isolated Co₂₊₂ single-atom site on nitrogen-doped carbon to activate PMS with 98.89% ¹O₂ generation selectivity [17]. Yang et al. modulated a curved Fe-N₄ site on a nanodiamond surface achieving outstanding activity on tetracycline degradation and near 100% selectivity of ¹O₂ [18]. Other M-N₄ SACs such as CoPc/G-NH₂ [19] and Zn-N₄ [20] were also tailored to improve the production of ¹O₂. Despite this, these catalysts with well-supported and symmetrical configurations of M-N₄ might not be optimal for catalytic activity in Fenton-like activity as well as the corresponding ¹O₂ selectivity [21]. Therefore, manipulating the coordination environment and local electronic structure of SACs, while elucidating the structure-property relationship of the single-atom sites, is crucial for the development of efficient Fenton-like catalysts and enhancement of ROS generation selectivity.

Owing to the properly defined and adaptable single-atom active sites, SACs have been widely modified at the atomic level to promote their catalytic performance, which mainly includes the following two pathways. (i) Coordination number regulation. Some researchers have reported that the coordination number was closely related to the electronic density of the single-atom sites, therefore governing their Fenton-like catalytic performance. For instance, Liang et al. revealed that lower coordination numbers contributed to the accumulation of charge density on the unsaturated single-atom site by analyzing the synthesized Co-N₂/3/4 [22]. Under such guidance, Fe-N₅ [23], Fe-N₆ [24], and Co-N₃ [25] were fabricated and applied to boost Fenton-like reactions in organic pollutant elimination; (ii) Heteroatom modulation. Phosphorus (P) [26], sulfur (S) [27], and boron (B) [28,29] with weak electronegativity were recently employed to efficiently tune the geometrical and local electronic configuration of single-atom sites. Among these atom modulation engineering strategies, boron atoms tend to attract more attention due to their electric-deficient feature (χ_B (2.04) < χ_N (3.04)) and similar atomic radius (0.82 Å) compared to N atoms (0.70 Å) [30], which exhibit excellent property to regulate the electron density of catalytic metal sites while maintaining the basic topological structure of the nitrogen-doped sp² hybridized graphite. For instance, in our previous study, the first coordination shell of the Cu site was modulated with an electric-deficient B atom (Cu-O₂B) and achieved nearly 100% ¹O₂ generation selectivity [28]. Similarly, Co-N₃B₁ [29], Cu-N₂B₂ [31], and FeN₃B [32,33] were also developed for enhancing the d-band delocalization and readjusting the electron density via the asymmetric coordination structure construction through foreign atom doping. Therefore, based on the above analysis, simultaneous regulation in coordination number and local electronic structure via heteroatom doping of the single-atom sites probably benefits the ¹O₂ selective generation. Moreover, fully comprehending the underlying mechanism of local coordination effects is also conducive to the rational engineering of potent Fenton-like catalysts.

Furthermore, some recent studies only constructed a single configuration to describe the PMS adsorption behavior during the catalytic process theoretically to explain the preferential ¹O₂ generation mechanism [15,16,34]. However, sporadic studies have suggested that the adsorption selectivity of different terminal O atoms in PMS might influence the ¹O₂ generation selectivity, which was also closely related to the electronic structure of single-atom sites [13,26,35,36]. Therefore, constructing the structure-property relationship between the electronic microenvironment of active sites and the adsorption selectivity of different terminal O atoms in PMS is conducive to elucidating the ¹O₂ generation selectivity mechanism and providing an in-depth understanding of the PMS activation process.

Herein, the local electronic structure of the traditional Fe-N₄ site was precisely manipulated by introducing an electron-depletion B atom, and

a six-coordination Fe-based SACs with Fe-N₂B₄ configuration was manufactured. When applied in PMS-mediated Fenton-like reactions, the Fe-N₂B₄ catalyst exhibited superior catalytic performance on bisphenol A (BPA) degradation (96.6%) for PMS activation with high ¹O₂ generation selectivity (98.68%). Experiments and theoretical simulations proved that the Fe valence situation in Fe-N₂B₄ configuration was tuned higher than that of the traditional Fe-N₄ site, whilst exhibiting different adsorption selectivity of terminal O atoms in PMS and resulted in the preferential ¹O₂ production. Density functional theory (DFT) calculations further clarified that a moderate d-band center for suitable binding strength of PMS and lower energy barrier in coordinates generation contributed to excellent catalytic performance and ¹O₂ selectivity. This work validates the heteroatom doping engineering a proven approach to precisely modulate the electronic structure of single-atom sites for ¹O₂ selectively generation in Fenton-like reactions, bringing an in-depth understanding between coordination environment and catalytic activity and guiding the rational future design of superior SACs applied in environment remediation.

2. Materials and methods

2.1. Material preparation

The Fe-based SACs with the Fe-N₂B₄ configuration was prepared via a two-step calcination strategy. Firstly, a typical Metal-Organic Framework (MOF), MIL-88A(Fe), was prepared via a hydrothermal strategy of a prior study [37], which was employed as the iron source mainly due to its high content of iron and property to spatially isolate metal ions using ligands and prevent metal agglomeration during calcination. Specifically, 20 mmol hydrated ferric chloride (FeCl₃·6 H₂O) and 20 mmol fumaric acid (FA) were immersed in 150 mL deionized (DI) water at 60 °C as the precursor, followed by transferring to a Teflon reactor (200 mL). Then, the solution was heated at 65 °C for 12 h and rinsed with DI water and ethanol a couple of times to remove the excess iron ions and FA. The brownish-red product was obtained after drying at 60 °C under vacuum overnight. Secondly, 1 g MIL-88A(Fe) was fully grounded with 2 g melamine and transferred into a tubular furnace for the first-step calcination at 600 °C under N₂ flow for 2 h with a heating rate of 5 °C min⁻¹. The resultant product (labeled as FeN_x-600, where 600 represents the calcination temperature) was collected after cooling down to room temperature. Additionally, as a contrast, the metal-free NC catalyst (NC-T, T represents the calcination temperature) was prepared using the same approach without the addition of MIL-88A(Fe). In the second-step calcination, 2 g boron acid was fully mixed with the synthesized FeN_x-600 catalyst (1 g) and reheated at 600 °C under N₂ flow for another 1 h with a ramp rate of 5 °C min⁻¹. The metal-free BCN catalyst was prepared by using NC-600 instead of FeN_x-600 in the second-step calcination. DI water at 70 °C was employed to eliminate the remaining boron acid in the mixture. After drying at 60 °C overnight, the black powder was obtained and labeled as FeN_x-B-2 (2 represents the mass ratio of boron acid and FeN_x-600 catalyst).

The details of chemicals, characterization, catalytic activity evaluation, and analysis methods were listed in Text S1-S4 and Table S1-S2 in the [supporting information](#).

2.2. Theoretical calculation method

First-principles-based calculations were performed based on an open-source CP2K package with mixed Gaussian and plane-wave basis sets [38]. The norm-conserving Goedecker-Teter-Hutter pseudopotentials were chosen to describe the core electrons [39]. DZVP-MOLOPT-SR-GTH basis set was employed with the auxiliary plane-wave basis cutoff energy of 400 Ry [40]. The calculations used Perdew-Burke-Ernzerhof (PBE) exchange-correlation functional within the generalized gradient approximation (GGA) [41]. To prevent inter-layer interference, the vacuum layer was adjusted at about 15 Å. A

k -mesh of $2 \times 2 \times 1$ was used to sample the first Brillouin-zone. Grimme's DFT-D3(BJ) methodology was employed to describe the effect of van der Waals interactions between PMS and SACs [42]. For the structural optimizations the positions of all atoms were optimized until all forces on atoms were smaller than 4.5×10^{-4} hartree/bohr. The configurations were optimized with the Broyden-Fletcher-Goldfarb-Shanno (BGFS) algorithm with an SCF convergence criterion of 5.0×10^{-6} au. Bader charges were calculated to analyze the electron density distribution on Fe-N₄ and Fe-N₂B₄ configurations. Moreover, the Fukui index, highest occupied molecular orbital (HOMO) and lower unoccupied molecular orbital (LUMO) of BPA were analyzed by Multiwfn based on DFT calculation [43] at the RB3LYP/6-31 G (D) level.

The adsorption energy (E_{ads}) is estimated by the following formula:

$$E_{\text{ads}} = E_{\text{surface+ molecule}} - E_{\text{surface}} - E_{\text{molecule}} \quad (1)$$

Where $E_{\text{surface+ molecule}}$ represents the combined energy of the whole system. E_{surface} and E_{molecule} represent the energy of the configuration surface and the free molecules, respectively.

3. Results and discussion

3.1. Synthesis and structural characterization

The B-doped Fe-based single-atom catalyst with Fe-N₂B₄ configuration was successfully synthesized via a two-step calcination strategy (Fig. 1a), with boron acid and melamine serving as B and N sources for Fe single-atom coordination. The parameters of melamine mass ratio, calcination temperature, and B doping ratio were optimized as

illustrated in Text S5, Fig. S1-S6, and Table S3 in the supporting information. Among all the samples, FeN_x-B-2 was designated as the model catalyst because of its superior catalytic performance.

As shown in Fig. S7, the scanning electron microscope (SEM) images of FeN_x-B-2 revealed a porous structure with more nanopores than that of FeN_x-600, indicating that B decoration engineering significantly affected the morphology of FeN_x SACs and exposed more active sites contributing to catalytic process [44]. The transmission electron microscopy (TEM) illustrated that FeN_x-B-2 and FeN_x-600 were layered without obvious agglomerates of iron nanoparticles and clusters (Figs. 1b-1c and Fig. S8). Iron atom dispersion was investigated using an aberration-corrected high-angle annular dark-field scanning transmission electron microscope (AC-HAADF-STEM). As depicted in Fig. 1d and S9, the isolated bright spots were assigned to the iron single atoms, which were anchored to the nitrogen-doped carbon substrate. It verified the successful atomic dispersion of iron both in FeN_x-600 and FeN_x-B-2. In addition, the inductively coupled plasma mass spectrometer (ICP-MS) measurement illustrated that the actual Fe content of FeN_x-600 and FeN_x-B-2 were 8.46 and 12.03 wt%, respectively, validating the high loading of Fe single atoms. Furthermore, C, B, N, and Fe atoms were distributed uniformly throughout FeN_x-B-2, as evidenced by the energy-disperse spectroscopy (EDS) mapping images (Fig. 1e). Collectively, the above evidence supports the formation of Fe single-atom sites both in FeN_x-600 and FeN_x-B-2.

As displayed in Fig. S10, the X-ray diffraction (XRD) patterns of FeN_x-600 and FeN_x-B-2 single atom catalyst showed only one characteristic peak at 27.7° assigned to graphite (JCPDS No. 41-1487), indicating that no crystalline iron or iron oxide species were generated.

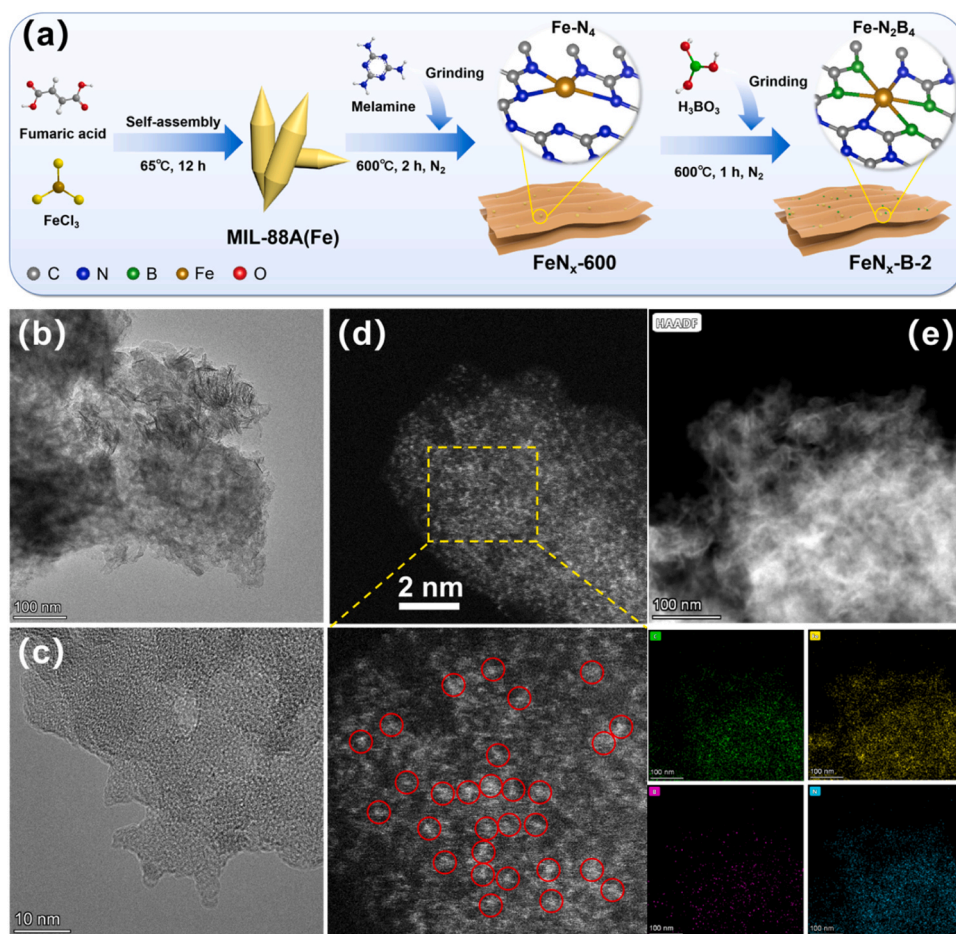


Fig. 1. Morphology characterization. (a) Schematic diagram of the preparation route of FeN_x-B-2; (b-c) HRTEM images; (d) aberration-corrected HAADF-STEM image; (e) EDS mapping images of FeN_x-B-2.

Notably, when the mass ratio of boron acid/ $\text{FeN}_x\text{-600}$ ranged from 0.1 to 2.0, a characteristic peak located at 35.8° was observed, while there was no obvious peak appeared in $\text{FeN}_x\text{-B-5}$. It was assigned to the (311) crystal plane of BN (JCPDS No. 51-0779) [12], suggesting the successful B doping in $\text{FeN}_x\text{-B-2}$ during the second-step calcination process. Additionally, the Fourier transform infrared spectrometer (FTIR) spectrum (Fig. S11) of $\text{FeN}_x\text{-600}$ and $\text{FeN}_x\text{-B-2}$ was investigated. Specifically, the peaks at ~ 1410 and 1580 cm^{-1} were assigned to C-C/C-O and C=C/C=N groups, confirming the basic skeleton of N-doped carbon was maintained after B doping in $\text{FeN}_x\text{-600}$. A slight peak at 1166 cm^{-1} corresponding to the C-B/B-O bond also validated the presence of B atoms [45]. Moreover, Raman spectra were utilized to explore the structural defects of the synthesized SACs, of which two typical characteristic peaks at 1352 cm^{-1} (D band) and 1585 cm^{-1} (G band) were identified (Fig. S12). Generally, the D band reflected the defect-induced features, whilst the G band represented the graphitization of sp^2 hybridized carbon [26]. Apparently, $\text{FeN}_x\text{-B-2}$ (1.37) exhibited significantly higher I_D/I_G values than $\text{FeN}_x\text{-600}$ (1.26), confirming that B decoration engineering resulted in more defects and disorder structures on the N-doping carbon substrate. The type-IV N_2 adsorption-desorption isotherm curves and associated pore size curves (Fig. S13) validated the

existence of micro and mesopores architecture of $\text{FeN}_x\text{-600}$ and $\text{FeN}_x\text{-B-2}$. As depicted in Table S4, the surface area of $\text{FeN}_x\text{-B-2}$ ($41.5\text{ m}^2/\text{g}$) was 4.2 times larger than that of $\text{FeN}_x\text{-600}$ ($9.9\text{ m}^2/\text{g}$), which was in accordance with the SEM results. The average pore size of $\text{FeN}_x\text{-B-2}$ (9.0 nm) was also higher than that of $\text{FeN}_x\text{-600}$ (7.7 nm). It illustrated that B decoration within the framework resulted in more porous architecture, enhancing the surface area and the pore size of $\text{FeN}_x\text{-600}$.

To identify the chemical state and electronic structures of the SACs, X-ray photoelectron spectroscopy (XPS) was performed (Fig. S14a). In the C1s spectra (Fig. S14b), the peaks related to C-C species (284.8 eV) exhibited a clear intensity increase in $\text{FeN}_x\text{-B-2}$, whilst C=N species (288.0 eV) was found to be lower than that in $\text{FeN}_x\text{-600}$ [46], illustrating the successful modification of B atoms on N doped sp^2 -hybridized carbon substrate. The N 1s signals could be fitted into five peaks at 398.5, 399.7, 400.5, 401.3, and 404.5 eV (Fig. 2a), which were assigned to pyridinic N, Fe-N, pyrrole N, graphite N and oxidized N, respectively [46,47]. It was noteworthy to mention that the ratio of pyridinic N in $\text{FeN}_x\text{-B-2}$ (61.0%) decreased compared to $\text{FeN}_x\text{-600}$ (76.3%), along with the significant emergence of Fe-N species (20.1%), suggesting that B atoms substituted part of pyridinic N and optimized the coordination

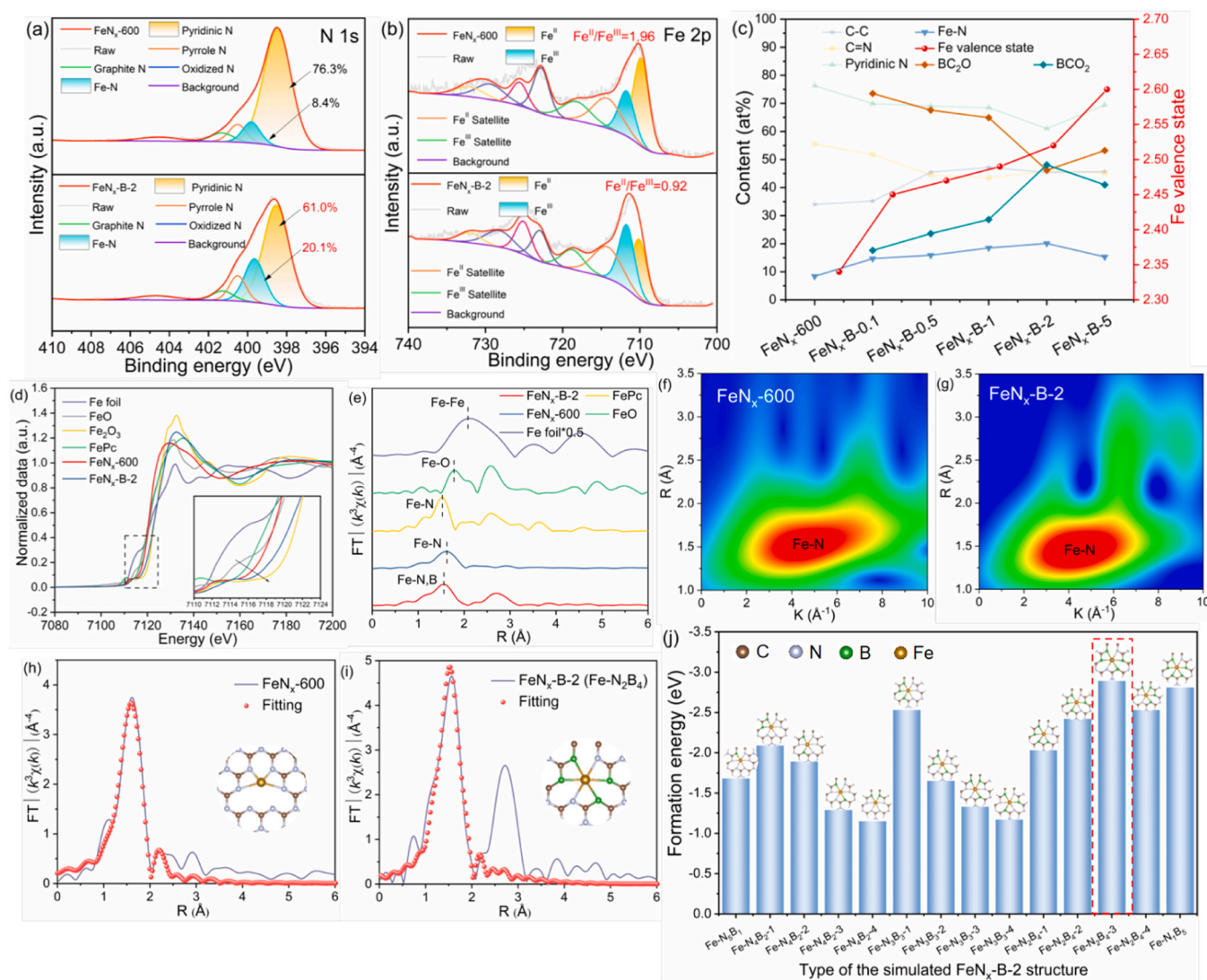


Fig. 2. Coordination environment of (a) N 1s and (b) Fe 2p XPS spectra of $\text{FeN}_x\text{-600}$ and $\text{FeN}_x\text{-B-2}$; (c) the content of C, N and B functions and the Fe valence state of the catalysts; (d) normalized Fe K-edge XANES spectra of Fe foil and other Fe-based samples; (e) FT-EXAFS spectra of $\text{FeN}_x\text{-600}$, $\text{FeN}_x\text{-B-2}$, FePc , Fe_2O_3 and Fe foil; Fe K-edge WT-EXAFS plots of (f) $\text{FeN}_x\text{-600}$ and (g) $\text{FeN}_x\text{-B-2}$; the FT-EXAFS R-space fitting curve of (h) $\text{FeN}_x\text{-600}$ (Fe-N_4) and (i) $\text{FeN}_x\text{-B-2}$ ($\text{Fe-N}_2\text{B}_4$); (j) the formation energies of all the possible B-doped Fe-based SACs configurations.

environment on the substrate, thereby enhancing the Fe single-atom sites. The Fe 2p spectra (Fig. 2b) revealed that B decoration significantly decreased the $\text{Fe}^{\text{II}}/\text{Fe}^{\text{III}}$ ratio from 1.96 to 0.92, whilst $\text{FeN}_x\text{-B-2}$ also displayed an upshift to higher binding energy and the spin-orbit splitting (15.4 eV) was larger than that of $\text{FeN}_x\text{-600}$ (13.8 eV) (Fig. S15), indicating that $\text{FeN}_x\text{-B-2}$ possessed a higher oxidized iron catalytic centers with lower charge density state [48] due to the doping of B atoms. The correlation of B doping content, functional groups, and Fe valence state across all B-doped Fe-based SACs was further investigated, demonstrating that B doping content exhibited a significant direct trend with Fe valence state (Fig. 2c, Fig. S16 and Table S5-S8), of which the average Fe valence state increased from 2.34 ($\text{FeN}_x\text{-600}$) to 2.52 ($\text{FeN}_x\text{-B-2}$). Moreover, the highest Fe-N content was achieved in $\text{FeN}_x\text{-B-2}$. The appropriate amount of B doping could raise the Fe-N content mainly due to the gasification of carbon mediated by O atoms in boron acid and the decrease of C content. However, excessive B doping ($\text{FeN}_x\text{-B-5}$) possibly damaged the topological framework and six-coordination environment of Fe single atom sites via extra-gasification of the carbon layer, which resulted in the decrease of Fe-N content (15.3%). The results illustrated that proper B doping could enhance the Fe catalytic sites effectively. Noting that, the proportion of BC_2O located at 191.4 eV was higher than that of BCO_2 at 192.6 eV all through the B modification process (Fig. S16d) [49], indicating that the BC_2O group might be dominant in B-doped Fe-based SACs and involved in Fe single-atom sites coordination.

3.2. Local coordination environment of Fe single-atom site analysis

X-ray absorption fine structure (XAFS) measurements were performed to determine the potential chemical state and local coordination environment of Fe in $\text{FeN}_x\text{-600}$ and $\text{FeN}_x\text{-B-2}$. As depicted in Fig. 2d, the normalized Fe K-edge X-ray adsorption near edge structure (XANES) spectra revealed that the Fe-rising edges in both $\text{FeN}_x\text{-600}$ and $\text{FeN}_x\text{-B-2}$ located between FeO and Fe_2O_3 , illustrating that the valence state of the Fe was intermediate between Fe(II) and Fe(III) [50], as further evidenced by a linearly fitted valence state of + 2.04 and + 2.28, respectively (Fig. S17a) [51]. This observation showed a good agreement with the Fe 2p XPS spectra. Besides, compared to $\text{FeN}_x\text{-600}$, the rightward-shift rising pre-edge and enhanced white-line peak in $\text{FeN}_x\text{-B-2}$ also suggested the rearrangement of charge polarization of Fe single atoms upon B doping [52]. As shown in Fig. 2e, the Fourier-transformed k^3 -weighted extended XAFS (FT-EXAFS) spectrum indicated the solitary Fe single atoms in $\text{FeN}_x\text{-600}$ and $\text{FeN}_x\text{-B-2}$ due to the absence of the Fe-Fe scattering path (at 2.12 Å) in contrast to Fe foil. This was also in line with the wavelet transform (WT)-EXAFS results (Figs. 2f-2g and Fig. S17b), in which the maximum intensity of $\text{FeN}_x\text{-600}$ and $\text{FeN}_x\text{-B-2}$ was clearly separated from that of Fe foil (7.7 Å^{-1}). A feature peak at 1.59 Å for $\text{FeN}_x\text{-600}$ in FT-EXAFS was located more closely to the backscattering of Fe-N (1.53 Å, Fe-N_4 , FePc) instead of Fe-O (1.78 Å, FeO) (Fig. 2e) [24]. Moreover, the center of $\text{FeN}_x\text{-B-2}$ (1.56 Å) exhibited a slight negative shift in comparison to that of $\text{FeN}_x\text{-600}$ after B doping. Consistent with the FT-EXAFS results, the maximum intensity $\text{FeN}_x\text{-600}$ (5.7 Å^{-1}) in WT-EXAFS was located close to Fe-N (FePc , 4.9 Å^{-1}) and away from Fe-O (FeO, 2.8 Å^{-1}), whilst the maximum intensity of $\text{FeN}_x\text{-B-2}$ (4.6 Å^{-1}) displayed a leftward shift (Figs. 2f-2g and Fig. S17c-17d). These results indicated the isolated Fe single atoms distribution anchored on the sp^2 hybridized carbon substrate and the effective B atoms modulation in the Fe coordination microenvironment.

Quantitative least squares fitting of the FT-EXAFS curves was employed to confirm the first-shell coordination of the Fe atoms (Table S9). Depending on the results, $\text{FeN}_x\text{-600}$ exhibited a four-coordination number of Fe-N (4.4 ± 0.5) in a Fe-N_4 configuration (Fig. 2h), while Fe atoms in $\text{FeN}_x\text{-B-2}$ were in a six-coordination state (5.9 ± 0.5) with Fe-N/B bond at a distance of 2.03 Å (Fig. 2i), which explicitly evidenced the reconstruction of atomic structure in $\text{FeN}_x\text{-600}$

after B doping. To further verify the co-coordination structure of B/N atoms in $\text{FeN}_x\text{-B-2}$, an inverse analysis was conducted by simulating XANES curves of different $\text{Fe-N}_x\text{B}_y$ centers (x and y represent the coordination numbers of N and B atoms, respectively) (Table S9 and Fig. S18) with each optimized DFT models (Fig. 2j and Table S10) [8, 53]. Among the 14 possible simulated configurations, $\text{Fe-N}_2\text{B}_4\text{-3}$ (3 represents the different configuration type) exhibited the lowest formation energy (−2.89 eV) with reasonable R^2 (0.0116) in FT-EXAFS fitting analysis, representing a thermodynamically favorable and stable feature of this structure. In this $\text{Fe-N}_2\text{B}_4$ configuration, B atoms replaced part of pyridinic N sites for the coordination with Fe atoms, which also showed decent alignment with XPS results. The above results strongly validated the majority of Fe-N_4 and $\text{Fe-N}_2\text{B}_4$ coordination configurations for $\text{FeN}_x\text{-600}$ and $\text{FeN}_x\text{-B-2}$, respectively. Most importantly, it confirmed the effective construction of the B/N co-coordination environment of Fe single atoms experimentally and theoretically, achieving a simultaneous regulation in coordination number and local electronic structure via heteroatom doping.

3.3. PMS activation capacity

The oxidative degradation of BPA as a representative organic contaminant was employed to systematically investigate the PMS catalytic performance of $\text{FeN}_x\text{-600}$ and $\text{FeN}_x\text{-B-2}$. As depicted in Fig. 3a, PMS and $\text{FeN}_x\text{-600}$ and $\text{FeN}_x\text{-B-2}$ alone only resulted in 9.2%, 13.5%, and 17.7% of BPA removal in 30 min, respectively, demonstrating the limited oxidizability of PMS self-decomposition and contribution of the catalyst adsorption. The NC-600/PMS system and the BNC/PMS system displayed negligible catalytic performance (14.4% and 11.9%, respectively), ruling out the PMS activation process via N-doped carbon substrate and boron functional groups without Fe active sites. As expected, high catalytic performance was observed for $\text{FeN}_x\text{-600}$ and $\text{FeN}_x\text{-B-2}$ after PMS addition, as seen from the BPA degradation efficiency of 90.1% and 96.6%, respectively, whilst the specific activity increased from $0.0955 \text{ L min}^{-1} \text{ g}^{-1}$ for $\text{FeN}_x\text{-600}$ to $0.1245 \text{ L min}^{-1} \text{ g}^{-1}$ for $\text{FeN}_x\text{-B-2}$. Meanwhile, the PMS consumption of $\text{FeN}_x\text{-B-2}$ reached 62.3% compared to that of $\text{FeN}_x\text{-600}$ (17.5%), implying the variation of PMS activation pathways in these two systems (Fig. S19). The above results highlighted the key roles of B doping on Fe single atom site modulation toward enhanced BPA degradation of $\text{FeN}_x\text{-B-2}$. Notably, only a minor amount of Fe^{2+} for $\text{FeN}_x\text{-600}$ and $\text{FeN}_x\text{-B-2}$ was leached (0.35 and 0.44 mg L^{-1} , respectively) in the catalytic process, reaching the permitted limit of Fe (5 mg L^{-1}) based on the Environmental Quality (Sewage and Industrial Effluents) Regulation 1979 [46]. Leaching iron only accounted for less than 19.5% of BPA degradation (Fig. S20), excluding the contribution of Fe-based homogeneous catalysis on the BPA degradation.

More investigation was performed to reveal the origins of the enhanced activity of $\text{FeN}_x\text{-B-2}$ and further explore its structure-activity relationship. As depicted in Fig. S21a, the pseudo-first-order kinetic rate constant (k_{obs}) of the B-doped Fe-based SACs were found to have a linear correlation ($R^2 = 0.91$ and 0.92 , respectively) with the content of BC_2O and BCO_2 . Besides, the relationship between Fe valence state and Fe-N content and catalytic performance was also investigated in Fig. S21b. Under low B doping content, although the average Fe valence state increased, it did not significantly change the catalytic performance of the catalyst (Fig. S6a). When continue increasing the B doping content, the catalytic performance of $\text{FeN}_x\text{-B-1}$ and $\text{FeN}_x\text{-B-2}$ raised as the average valence state of Fe and Fe-N proportion increased, confirming that a certain amount of B doping could facilitate PMS activation and drive the BPA oxidative degradation. Notably, the decrease of k_{obs} of $\text{FeN}_x\text{-B-5}$ might be due to the loss of Fe-N sites (15.3%), proving the importance of rational modulation of Fe single-atom sites by B atoms. Other potential associations between the chemical structures and catalytic properties were also established (Fig. 3b), among which Fe valence state, Fe-N, BC_2O , and BCO_2 content exhibited relatively higher R^2 than

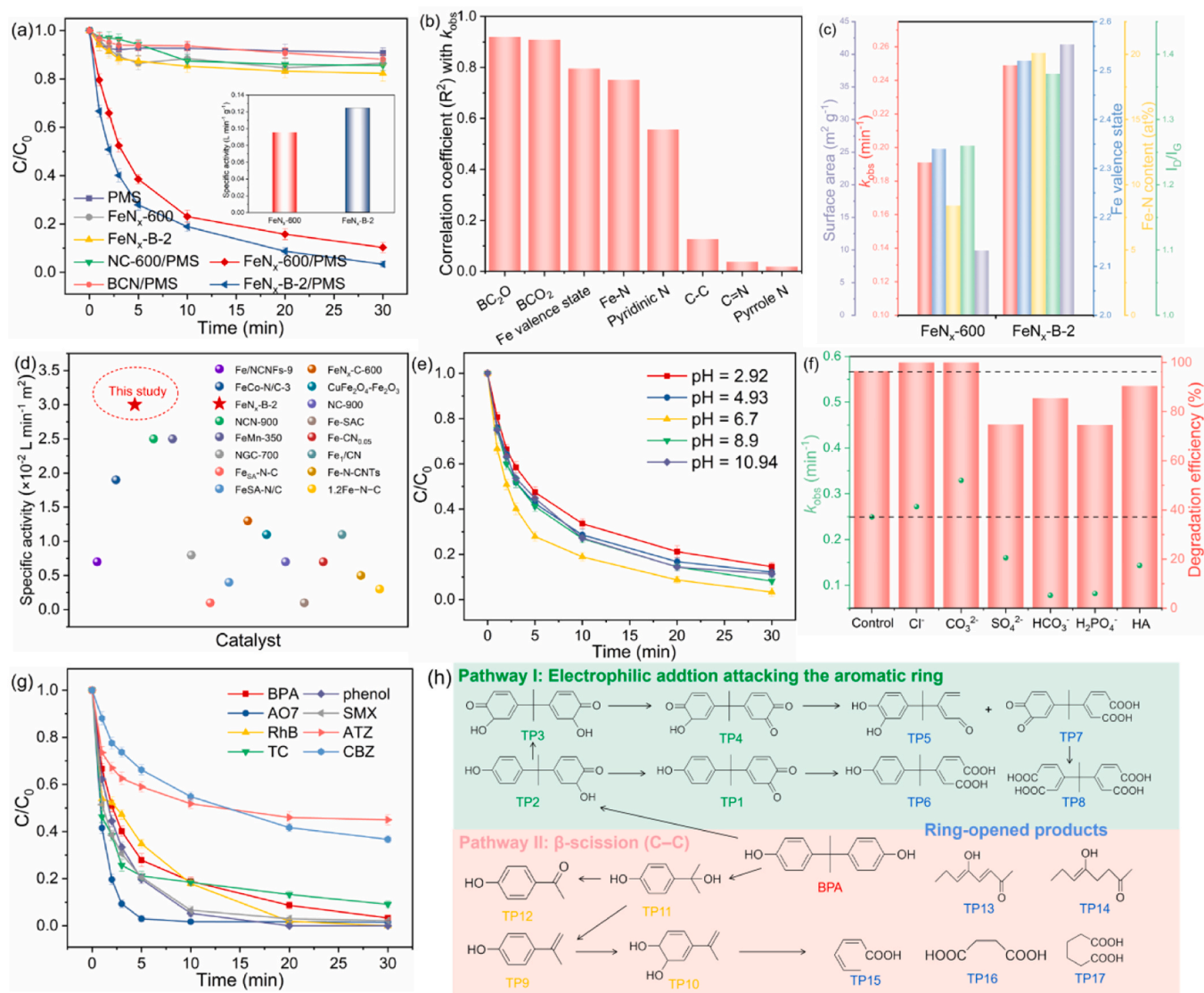


Fig. 3. Catalytic performance evaluation. (a) The BPA degradation performance in different systems; (b) the correlation between k_{obs} , different functional groups and Fe valence state; (c) the comparison of observed k_{obs} , surface area, Fe valence state, I_p/I_g and Fe-N content between FeN_x-600 and FeN_x-B-2; (d) specific activity comparison of organic pollutant degradation in the FeN_x-B-2/PMS system and other Fe-based carbon-derived SACs/PMS systems; (e) influence of pH, (f) co-existing anions and NOM on BPA degradation in the FeN_x-B-2/PMS system; (g) degradation efficiency in multiple organic pollutants in the FeN_x-B-2/PMS system; (h) proposed degradation pathways of BPA in the FeN_x-B-2/PMS system. Reaction conditions: [BPA]₀ = 20 mg L⁻¹, [PMS]₀ = 2.0 mM, [catalyst]₀ = 0.2 g L⁻¹, initial pH = 6.7.

other structures (C-C, C=N, pyridinic N, and pyrrole N), verifying the essential roles they played in the enhancement of the catalytic performance of FeN_x-B-2.

Therefore, according to the characteristics and catalytic results, the superiority of the catalytic performance of FeN_x-B-2 over FeN_x-600 might be due to: (i) more defects and disorder structures on carbon substrate after B doping for promoting ROS production; (ii) more Fe-N single-atom active sites and higher Fe valence state regulated by B atoms which attributed to optimizing the adsorption configuration of PMS; (iii) larger surface area caused by boron acid decomposition under high temperature which contributed to the molecule transfer in the catalyst (Fig. 3c). Moreover, the normalized k_{obs} (specific activity) of the FeN_x-B-2/PMS catalytic system was superior than most of existing heterogeneous Fe-based or carbon-derived catalysts reported previously (Fig. 3d and Table S11), substantiating the excellent PMS catalytic activity of FeN_x-B-2.

The degradation efficiency of BPA with various catalyst dosages was shown in Fig. S22. When the PMS dosage was fixed, increasing the

catalyst dosage would enhance the k_{obs} by providing more reactive sites for PMS activation. The highest specific activity (0.3 L min⁻¹ m⁻²) was observed at a catalyst dosage of 0.2 g L⁻¹, demonstrating the full utilization of reactive sites on the catalyst under this experiment condition. Excessive catalysts might lead to waste of the active sites and reduce the utilization of atoms in the case of a certain oxidant. Increasing PMS concentration also improved the catalytic efficiency (Fig. S23a). 2 mM PMS concentration resulted in an excellent BPA degradation efficiency (96.6%) compared to 1 mM (79.2%), whilst the increment of degradation efficiency was not significant by continuously increasing the PMS concentration (Fig. S23b), which was mainly due to the limited active sites for PMS activation and the effect of scavenging radicals by PMS under high concentration, thus 2 mM was chosen for further investigation. Fig. 3e revealed that the catalytic performance of FeN_x-B-2 was applicable at a wide pH range (2.92–10.94) with BPA removal efficiency higher than 85.5% (Fig. S24), which was beneficial for the treatment of practical wastewater. The slight decline in acid conditions might be due to that excessive H⁺ would bind with PMS and ROS and thereby suppress

the catalytic kinetics [54]. The weak inhibition also occurred in alkaline conditions, which was mainly due to the conversion of HSO_5^- to SO_5^{2-} ($\text{pK}_a = 9.4$) and target organic pollutant BPA to BPA^- , thus preventing the catalytic process [55]. Moreover, the hyper-acidic or hyper-alkaline environment also diminished the BPA adsorption capacity of the active sites on the catalyst (Fig. S24c), influencing the BPA adsorption and degradation efficiency during the Fenton-like reaction [56].

The impact of several inorganic anions and natural organic matter (NOM) on the anti-interference capacity of $\text{FeN}_x\text{-B-2}$ was also investigated (Fig. 3f and Fig. S25), in which Cl^- and CO_3^{2-} exhibited a higher k_{obs} , and a slight decay on k_{obs} was observed in the presence of HCO_3^- , SO_4^{2-} , H_2PO_4^- and HA. According to the previous literature, the enhanced catalytic performance on BPA degradation with Cl^- addition was possibly due to the generation of active HClO by Cl^- [23], whilst CO_3^{2-} could react with H^+ produced by the decomposition of PMS in the non-radical pathway and promoted the singlet oxygen generation [10]. The addition of HCO_3^- increased the pH of the solution, which had a negative impact on BPA degradation, while H_2PO_4^- could form metal complexes with Fe-based SACs on the catalyst surface and inhibited the catalytic process [3]. Despite slowing down the degradation rate, HCO_3^- , SO_4^{2-} , H_2PO_4^- and HA failed to dramatically reduce the BPA degradation efficiency in 30 min by $\text{FeN}_x\text{-B-2}$, illustrating the free radicals' negligible contribution to BPA removal. More importantly, the BPA degradation efficiency could be also achieved at over 85% in tap water and river water systems (Fig. S26), further indicating its adaptability in practical wastewater.

To investigate the catalytic performance of $\text{FeN}_x\text{-B-2}$ on different organic contaminants, other pollutants including acid orange 7 (AO7), tetracycline (TC), phenol, Rhodamine B (RhB), and sulfamethoxazole (SMX) were also evaluated (Fig. 3g and Fig. S27), achieving a degradation efficiency of over 90% in 30 min. Conversely, atrazine (ATZ) and carbamazepine (CBZ) exhibited only approximately 55.0% and 63.3%, respectively. The selective oxidation of various organic contaminants might be intimately related to the different electron-donating/withdrawing abilities of the pollutant molecule, which further suggested that the selective non-radical pathway might be dominant in the $\text{FeN}_x\text{-B-2/PMS}$ system. Furthermore, $\text{FeN}_x\text{-B-2}$ retained good catalytic activity with over 75% BPA degradation efficiency in the first four cycles (Fig. S28a), while the crystal structure and FTIR spectra also remained stable (Fig. S28b-S28c). The decline of the catalytic performance was presumably due to the incorporation of BPA intermediates on the active sites [57,58]. The catalytic activity of deactivated $\text{FeN}_x\text{-B-2}$ could be regenerated by thermal treatment as previously reported due to the decomposition of intermediates [57], and the iron proportion (11.56 wt %) and leaching content (0.31 mg L^{-1}) remained stable after repeated, suggesting that the stability and regeneration feature of $\text{FeN}_x\text{-B-2}$ could support the cycle utilization in practical application.

The total organic carbon (TOC) removal efficiency achieved 44.3% in 90 min, demonstrating the effective mineralization ability of the $\text{FeN}_x\text{-B-2/PMS}$ system (Fig. S29). According to the detected BPA intermediates by Liquid chromatography-mass spectrometry (LC-MS) (Table S12), two possible degradation pathways including (i) electrophilic addition on the aromatic ring and (ii) β -scission (C-C) were proposed in Fig. 3h, which resulted in ring-opened products and further oxidation into CO_2 and H_2O [59]. Moreover, the attacking sites of BPA were further confirmed by HOMO, LUMO orbitals, and Fukui index analysis, demonstrating the rationality of the proposed degradation pathway (Fig. S30).

3.4. ROS identification and catalytic mechanism

Heteroatom modulation engineering has proved to be an effective strategy to regulate the coordination environment of the single-atom catalytic active site for selective ROS generation [26,28]. To determine the dominant ROS involved in BPA degradation, radical quenching tests were carried out. Tert-butanol (TBA) was used as a quencher for

hydroxyl-OH, whilst methanol (MeOH) was employed to quench-OH and SO_4^\cdot . P-benzoquinone (p-BQ), furfuryl alcohol (FFA), and β -carotene were selected as quenchers for superoxide radical (O_2^\cdot) and $^1\text{O}_2$, respectively (Fig. 4a and Fig. S31a-S31b) [7,60]. Considering the possible interference of common $^1\text{O}_2$ inhibitors (FFA and β -carotene) on the contribution of $^1\text{O}_2$ during the catalysis process by consuming PMS and competing with organics with adsorption sites on the catalysts [56], the appropriate $^1\text{O}_2$ inhibitors concentration was determined in advance (Fig. S31c). In the $\text{FeN}_x\text{-600/PMS}$ system, the BPA degradation was significantly inhibited when adding the quenchers of -OH, SO_4^\cdot , and O_2^\cdot , indicating the presence of multiple ROS generated from PMS which contributed to the contaminant elimination. However, in the $\text{FeN}_x\text{-B-2/PMS}$ system, the inhibition of FFA and β -carotene remained at over 50%, while TBA, MeOH, and p-BQ showed relatively limited suppression in the catalytic process, which preliminarily revealed that $^1\text{O}_2$ might be the dominant ROS in the reaction. As the previous literature reported, $^1\text{O}_2$ exhibited a faster reaction rate constant with BPA ($k(^1\text{O}_2, \text{BPA}) = 2.15 \times 10^8 \text{ M}^{-1} \text{ s}^{-1}$) than ATZ ($k(^1\text{O}_2, \text{ATZ}) = 2 \times 10^6 \text{ M}^{-1} \text{ s}^{-1}$), which was aligned with the degradation results (Fig. 3g), strongly demonstrating that $^1\text{O}_2$ was predominantly responsible for BPA oxidative removal in the $\text{FeN}_x\text{-B-2/PMS}$ system [61].

To further validate the ROS generated during PMS activation by $\text{FeN}_x\text{-B-2}$, electron paramagnetic resonance (EPR) characterization was conducted with 5,5-dimethyl-1-pyrroline N-oxide (DMPO) and 2,2,6,6-tetramethylpiperidine (TEMP) as trapping agents (Fig. 4b-d). No signals were identified in the sole PMS system. A weak feature peak of DMPO-OH (intensity ratio of 1:2:2:1) and DMPO- SO_4^\cdot (intensity ratio of 1:1:1:1:1:1) adducts were recorded in the $\text{FeN}_x\text{-600/PMS}$ system due to the production of -OH and SO_4^\cdot [41], whilst no significant indications were obtained in the $\text{FeN}_x\text{-B-2/PMS}$ system, excluding the presence of these two radicals. Strong triplet EPR signals corresponding to $^1\text{O}_2$ were observed in both catalytic systems [62], and the intensity of TEMP- $^1\text{O}_2$ in the $\text{FeN}_x\text{-B-2/PMS}$ system was dramatically improved in comparison to the $\text{FeN}_x\text{-600/PMS}$ system (Fig. 4c), which strongly proved that $^1\text{O}_2$ was selectively generated and prevailed in BPA degradation in the $\text{FeN}_x\text{-B-2/PMS}$ system. Notably, the DMPO- O_2^\cdot (peak with intensity ratio of 1:1:1:1) signal in $\text{FeN}_x\text{-B-2}$ was relatively weaker than that in $\text{FeN}_x\text{-600}$ (Fig. 4d), suggesting a different pathway for $^1\text{O}_2$ generation without O_2^\cdot in $\text{FeN}_x\text{-B-2}$ and the existence of O_2^\cdot did not contribute significantly to the BPA degradation. Moreover, the BPA degradation was conducted in deuterioxide (D_2O) to further verify the presence of $^1\text{O}_2$, because the lifetime of $^1\text{O}_2$ in D_2O (22–70 μs) was 10 times higher than that in H_2O (2.9–4.6 μs) [23]. As depicted in Fig. S32, the intensity of $^1\text{O}_2$ in the EPR spectrum was obviously enhanced, whilst its k_{obs} also increased from 0.249 min^{-1} to 0.280 min^{-1} , strongly confirming the production of $^1\text{O}_2$ in the $\text{FeN}_x\text{-B-2/PMS}$ system.

Previous studies have reported that direct electron transfer might also mediate organic degradation when PMS and organic pollutants co-existed on the surface of the catalyst [45]. Therefore, an open-circuit potential test (OCPT) was employed to verify the electron transfer progress (Fig. 4e). After the injection of PMS 200 s after the reaction, the open-circuit potential of $\text{FeN}_x\text{-600}$ and $\text{FeN}_x\text{-B-2}$ increased significantly, which was attributed to the electronic redistribution caused by the adsorbed PMS on the Fe active sites, producing the catalyst-PMS complex with high redox potential. The sequential incorporation of BPA provoked a remarkable drop in the potential, while the blank test exhibited barely detectable variance, verifying the electron transfer between BPA, PMS, and both catalysts. Interestingly, the potential of $\text{FeN}_x\text{-B-2}$ declined and gradually rose back to the original level after the addition of BPA, whilst $\text{FeN}_x\text{-600}$ declined to 1.44 V at the steady state. It might be attributed to the moderate PMS adsorption capacity of $\text{FeN}_x\text{-B-2}$ and the rapid desorption of sub-stable PMS- $\text{FeN}_x\text{-B-2}$ surface complexes, which boosted the PMS activation and catalytic process. Moreover, the higher current density of $\text{FeN}_x\text{-B-2}$ demonstrated that PMS preferred to donate electrons to the catalyst surface, in which PMS decomposed into SO_5^\cdot and accounted for $^1\text{O}_2$ generation [9].

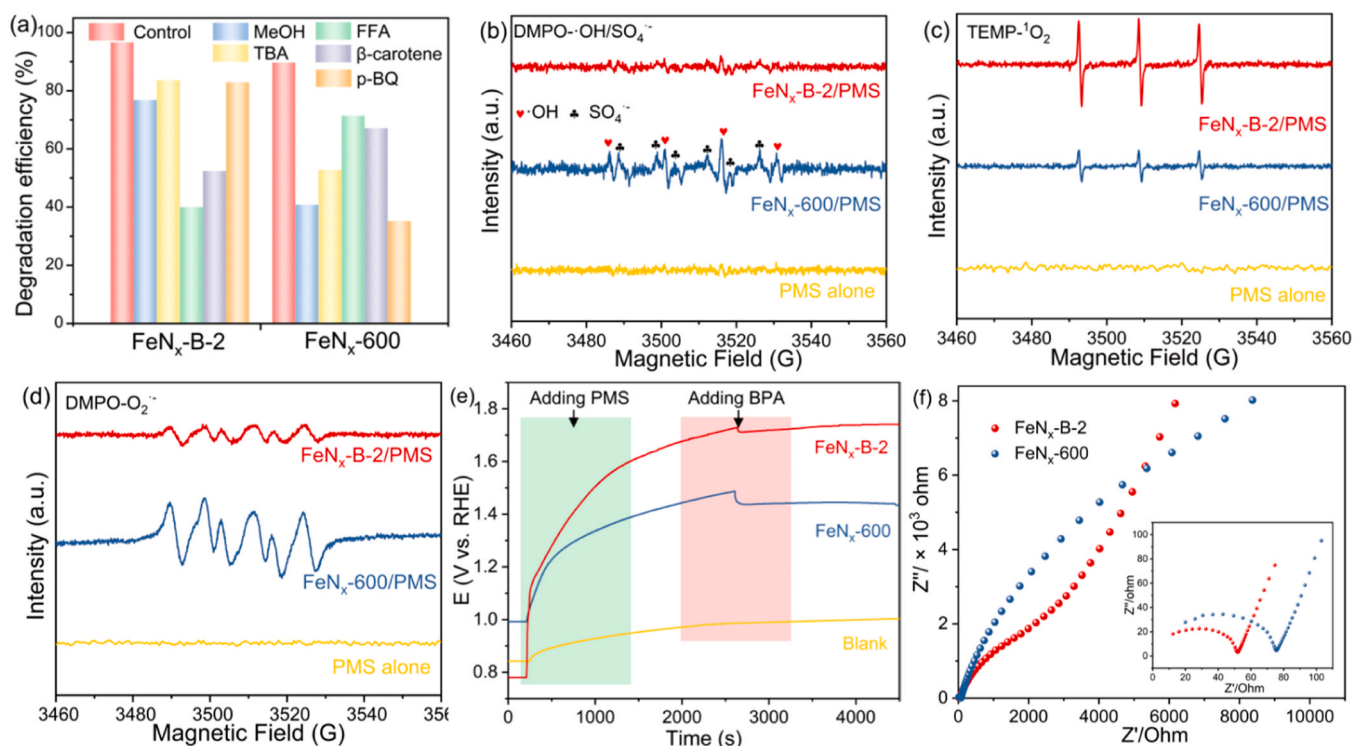


Fig. 4. (a) Effects of the ROS quenching agents on BPA degradation in the FeN_x-600/PMS and FeN_x-B-2/PMS systems; EPR spectrum of the different systems captured by DMPO and TEMP for detection of (b) $\cdot\text{OH}$ and $\text{SO}_4^{\cdot-}$, (c) $\text{O}_2^{\cdot-}$, and (d) $^1\text{O}_2$; (e) the open-circuit potential of FeN_x-600 and FeN_x-B-2 with addition of PMS solution (2 mM); (f) EIS plots of FeN_x-600 and FeN_x-B-2. Reaction conditions: $[\text{BPA}]_0 = 20 \text{ mg L}^{-1}$, $[\text{PMS}]_0 = 2.0 \text{ mM}$, $[\text{catalyst}]_0 = 0.2 \text{ g L}^{-1}$, $[\text{MeOH}, \text{TBA}] = 200 \text{ mM}$, $[\text{FFA}, \text{p-BQ}] = 10 \text{ mM}$, $[\beta\text{-carotene}] = 0.4 \text{ mM}$, initial pH = 6.7.

Electrochemical impedance spectroscopy (EIS) and Tafel polarization curves (Fig. 4f and Fig. S33) showed that FeN_x-B-2 possessed a lower charge transfer resistance than FeN_x-600, illustrating that the B modulated Fe single atom site increased the electron transfer efficiency of the carbon substrate.

Recent studies have shown that high-valence metal species might be potential reactive species and play important roles in SACs-based catalytic systems [63,64]. Due to the specific oxygen transfer reaction between methyl phenyl sulfoxide (PMSO) and high-valence metal species, which would result in the generation of phenyl methyl sulfone (PMSO₂), a PMSO probe was employed to ascertain the existence of high-valence iron species [65]. As shown in Fig. S34a–34b, the high-performance liquid chromatography (HPLC) spectra demonstrated that the peak of PMSO₂ (4.62 min) significantly enhanced in the FeN_x-600/PMS system, whilst almost no signal was obtained in the FeN_x-B-2/PMS system. Moreover, the suppression of BPA degradation after the addition of dimethylsulfoxide (DMSO) in the FeN_x-B-2/PMS system was insignificant (Fig. S34c–34d), but non-negligible in the FeN_x-600/PMS system. It demonstrated the absence of high-valence iron species on B-regulated Fe single-atom sites of the FeN_x-B-2 surface, which was consistent with other SACs with modulated single-atom sites [19,56]. The disappearance of high-valence iron species in FeN_x-B-2 mainly because B doping influenced the traditional N-coordination environment of Fe single atoms directly, changed the electron occupation situation of d-orbitals of Fe atoms, and altered the adsorption behavior between active sites and O atoms. These results suggested that the precise modulation of the Fe coordination micro-environment and electronic structure by B atoms could alter the produced reactive species during catalysis and affect the Fenton-like reaction process.

Next, the steady-state concentrations of the major ROS ($\cdot\text{OH}$, $\text{SO}_4^{\cdot-}$, $\text{O}_2^{\cdot-}$ and $^1\text{O}_2$) in the catalytic systems were quantified by using benzoic acid (BA), nitrobenzene (NB), parachlorobenzoic-acid (p-CBA) and FFA as probe compounds [66,67] (Fig. S35), of which the second-order reaction

rate constants with BPA were shown in Table S2. The steady-state concentrations of ROS were calculated as depicted in Table S13 and Fig. 5a. In the FeN_x-600/PMS system, $\cdot\text{OH}$, $\text{SO}_4^{\cdot-}$ and $\text{O}_2^{\cdot-}$ were generated with a concentration of $5.13 \times 10^{-14} \text{ M}$, $5.74 \times 10^{-14} \text{ M}$, and $7.37 \times 10^{-13} \text{ M}$, respectively. For the FeN_x-B-2/PMS system, the yield of $[\cdot\text{OH}]_{\text{ss}}$ and $[\text{SO}_4^{\cdot-}]_{\text{ss}}$ decreased to $2.05 \times 10^{-14} \text{ M}$ and $1.28 \times 10^{-14} \text{ M}$, whilst $[\text{O}_2^{\cdot-}]_{\text{ss}}$ was only $3.66 \times 10^{-14} \text{ M}$ compared to that of FeN_x-600, indicating the remarkable PMS activation route transformation. Moreover, much higher $[\text{O}_2^{\cdot-}]_{\text{ss}}$ was obtained in the FeN_x-B-2/PMS system ($5.22 \times 10^{-12} \text{ M}$), which was 3.4 times than that in the FeN_x-600/PMS system ($1.54 \times 10^{-12} \text{ M}$). It demonstrated that $^1\text{O}_2$ generation was selectively enhanced on B atoms regulated Fe single-atom catalytic site in FeN_x-B-2, which accounted for more than 98.68% of the total ROS compared to that of 64.57% in the FeN_x-600/PMS system (Fig. 5b) and was competitive compared to other transition metal-based SACs applied for $^1\text{O}_2$ selectivity generation (Table S14).

Several experiments were conducted to investigate the origins of $^1\text{O}_2$ and the particular catalytic site on FeN_x-B-2. The BPA degradation in different atmospheres (N_2 , O_2 , and air) exhibited a slight difference (Fig. S36), illustrating that $^1\text{O}_2$ was generated through PMS activation instead of the dissolved oxygen in the solution. Then, oxalate and potassium thiocyanate (KSCN) were added to the FeN_x-B-2/PMS system as poisoning species and BPA removal was significantly inhibited [68], demonstrating that the atomic Fe was the specific catalytic sites responsible for PMS activation (Fig. 5c). To reveal the possible catalytic mechanism on the regulated Fe single-atom catalytic sites, the high-resolution XPS Fe 2p spectra of FeN_x-B-2 before and after used was investigated. As depicted in Fig. 5d, the two peaks at 710.9 and 724.5 eV were assigned to the binding energies of Fe 2p_{1/2} and 2p_{3/2}, respectively. Moreover, a careful deconvolution of the Fe 2p spectrum of FeN_x-B-2 revealed that the Fe species consisted of Fe²⁺ and Fe³⁺ with a ratio of 0.92 (Fig. 2b). The ratio of Fe²⁺/Fe³⁺ exhibited a significantly higher value (1.28) after the reaction, indicating that the Fe valence state

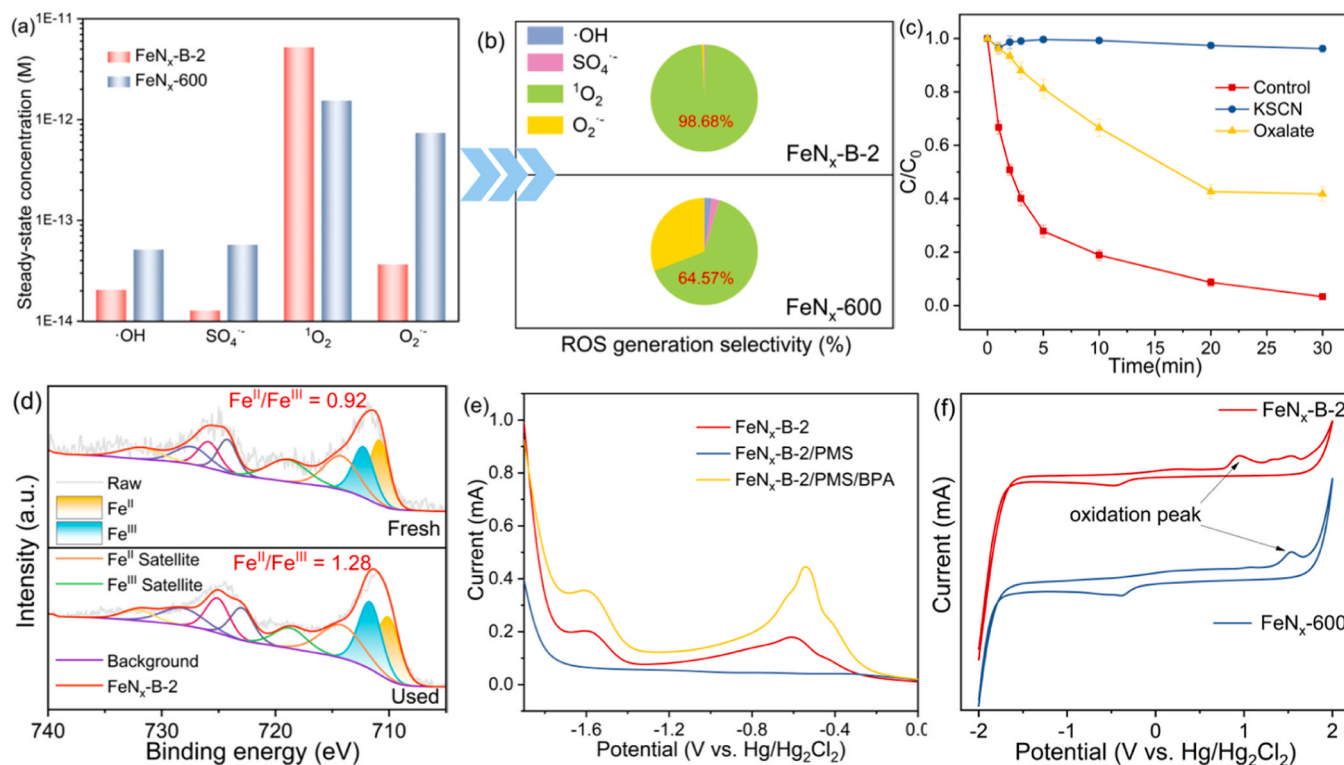


Fig. 5. (a) The steady-state concentrations and (b) generation selectivity of different ROS in BPA degradation in the FeNx-600/PMS system and FeNx-B-2/PMS system; (c) Fe catalytic sites identification by using poisoning species (KSCN and oxalate, 50 mM); (d) Fe 2p XPS spectrum of FeNx-B-2 before and after use; (e) LSV curves of FeNx-B-2 with and without BPA and PMS; (f) CV curves of FeNx-B-2 and FeNx-600. Reaction conditions: $[\text{BPA}]_0 = 20 \text{ mg L}^{-1}$, $[\text{PMS}]_0 = 2.0 \text{ mM}$, $[\text{catalyst}]_0 = 0.2 \text{ g L}^{-1}$, initial pH = 6.7.

decreased due to the electron gain of Fe sites from PMS.

The linear scanning voltammetry (LSV) profiles were further carried out to estimate the electron transfer process on Fe single-atom sites. Two distinct reduction peaks located at 0.61 V and 1.62 V were observed in the presence of FeNx-B-2 (Fig. 5e), whilst FeNx-600 only exhibited one reduction peak at around 0.47 V (Fig. S37), indicating higher oxidizability and electron acceptability of FeNx-B-2 during the reaction process [69]. Similarly, a lower oxidation peak potential of FeNx-B-2 was also obtained in cyclic voltammetry (CV) curves (Fig. 5f), further verifying its less reducibility due to the higher oxidation state [29,58]. Both systems showed a much smaller current fluctuation after PMS addition, implying the generation of PMS-catalyst composite on the surface Fe catalytic sites [59]. Noting that, the FeNx-B-2/PMS/BPA system exhibited a significant current increase with two similar reduction peaks, indicating the presence of electron transfer from BPA to PMS on the catalyst surface [70]. However, the reduction peak left-shifted to 0.68 V with negligible current variation in the FeNx-600/PMS/BPA system, suggesting that electron transfer might not be a major BPA oxidation pathway and PMS preferred to accept electrons from the catalyst in the FeNx-600/PMS system. In conclusion, the above analysis revealed that the Fe single atom catalytic site regulated by B atoms on FeNx-B-2 with higher oxidation state and electron transfer property was conducive to selectively $^1\text{O}_2$ generation because of the preference for accepting electrons from PMS instead of donating electrons for various ROS production.

3.5. Theoretical study of PMS activation mechanism on B-regulated Fe catalytic site

DFT calculations were further employed to determine the involved reaction mechanism of B-doping Fe-based SACs and explore the reason why the modulation of the Fe coordination environment by B atoms changed the catalytic mechanism at the atomic level. According to the

characterization of the Fe coordination number of FeNx-600 and FeNx-B-2, two models (Fe-N₄ and Fe-N₂B₄, respectively) were created as shown in Fig. 6a, which preserved the same triangular pore geometry as g-C₃N₄ and owned six potential coordination sites. The electron density distribution and Bader charges analysis showed that the introduction of B atoms altered the local electronic structure of Fe-N₂B₄, especially for Fe centers (Fig. 6b and Fig. S38). The calculated Bader charges in Fe-N₂B₄ (+0.95) were significantly higher than that of Fe-N₄ (+0.85) possibly due to the electron-deficient properties of B atoms, which was qualitatively aligned with the XANES and XPS results. The difference in the oxidation state of the Fe central site led to the different adsorption behavior between PMS and catalysts, thereby affecting the reaction mechanism. Previous studies have reported that the differential adsorption energy of O1 and O2 atoms in PMS adsorption configurations ($\Delta E_{\text{ads}} = E_{\text{ads-O1}} - E_{\text{ads-O2}}$) was favorably associated with the $^1\text{O}_2$ generation selectivity [28,35,36], which might be a $^1\text{O}_2$ selective generation descriptor. Therefore, several adsorption configurations between different O atoms of PMS and catalyst were established and analyzed as shown in Table S14. As depicted in Fig. 6c-d, the differential adsorption energy of O1 and O2 atoms in PMS dramatically increased the selectivity and steady-state concentration of $^1\text{O}_2$ as expected. The ΔE_{ads} of Fe-N₄ for O1 and O2 atoms in PMS was inferior (−0.07 eV), indicating that the Fe site in Fe-N₄ exhibited a relatively lower $^1\text{O}_2$ generation selectivity (64.57%) and steady-state concentration ($1.54 \times 10^{-12} \text{ M}$). Inversely, Fe-N₂B₄ demonstrated specific adsorption selectivity for O1 atoms in PMS molecules ($\Delta E_{\text{ads}} = -0.15 \text{ eV}$), with higher $^1\text{O}_2$ generation selectivity (98.68%) and steady-state concentration up to $5.22 \times 10^{-12} \text{ M}$, confirming the key role of B atoms modulation on ROS selectively generation.

The charge transfer between adsorbed PMS and catalyst was investigated using difference charge density (Fig. 6e) [28]. Remarkable charge density stacking between PMS and Fe-N₄ or Fe-N₂B₄ (electron accumulation, green region; electron depletion, blue region) was

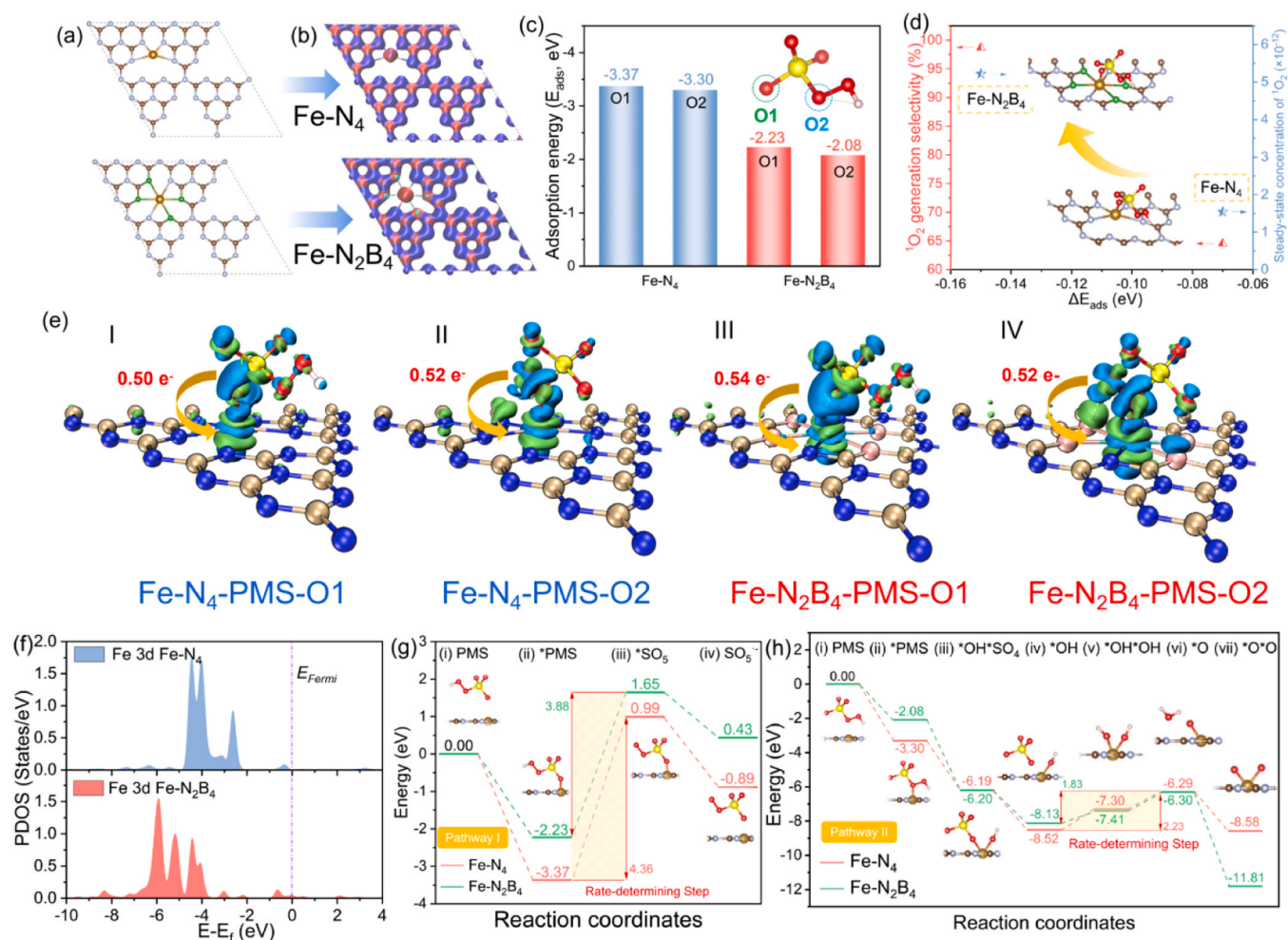


Fig. 6. Theoretical analysis of the catalytic mechanism. (a) The theoretical models of FeN_x-600 (Fe-N₄ configuration) and FeN_x-B-2 (Fe-N₂B₄ configuration); (b) the electron distribution of the two simulated configurations (red region represents electron-positive and blue region represents electron-negative); (c) the adsorption energy of PMS on FeN_x-600 (Fe-N₄ configuration) and FeN_x-B-2 (Fe-N₂B₄ configuration); (d) the relationship between the adsorption energy gap of O1/O2 of PMS and catalyst, ¹O₂ generation selectivity and the ¹O₂ steady-state concentration; (e) differential charge analysis on various adsorption configuration (green and blue region represents the electron accumulation and depletion, respectively); (f) PDOS of Fe 3d states in FeN_x-600 and FeN_x-B-2; (g-h) possible energy profiles of the two reaction pathways for the generation of ¹O₂.

observed, suggesting that the charges mainly migrated from PMS to Fe sites. The Fe sites in Fe-N₂B₄ exhibited a higher electron transfer amount compared to Fe-N₄, demonstrating its excellent electron transfer property. Noting that, the electron transfer amount of Fe-N₂B₄-PMS-O1 (0.54 e) was also higher than Fe-N₂B₄-PMS-O2 (0.52 e), illustrating that this adsorption configuration was more conducive to the ¹O₂ selectively generation. Moreover, as depicted in Fig. 6f, the projected density of states (PDOS) of the Fe center in Fe-N₂B₄ exhibited a negative shift and the d-band center was further away from Fermi Energy compared to Fe-N₄, which was conducive to the desorption of reaction intermediates and facilitated the next reaction step as well as promoting the k_{obs} (Fig. S39-S40) [19,56].

According to the previous works [8,26,34,35], ¹O₂ was mainly generated by the following two transformation pathways: (i) PMS-O1 was first adsorbed on the catalyst and produced *SO₅ after the breakage of the O-H bond, followed by ¹O₂ production after rapid self-reaction of *SO₅ after desorption; (ii) the adsorption of PMS-O2 resulted in the breakage of O-O bond and the generation of *SO₄ and *OH, followed by ¹O₂ production after complicated reactions between absorbed O-containing intermediates. To further distinguish the different selectivity towards reactive species of Fe-N₂B₄ and Fe-N₄, the change of energy for ¹O₂ formation in two typical pathways was investigated in Fig. 6g-h. In pathway I, both Fe-N₄ and Fe-N₂B₄ exhibited

a high energy barrier in the *SO₅ generation step, demonstrating that the generation of *SO₄ and *OH was more thermodynamically favorable. In spite of this, the energy barrier decreases from 4.36 eV for Fe-N₄/PMS system to 3.88 eV for Fe-N₂B₄/PMS system, showing the potential of Fe-N₂B₄ to promote the ¹O₂ generation process. In pathway II, the optimized energy diagram was PMS → *PMS → *SO₄ → *OH → *OH → *OH*OH → *O → *O*O. It was apparent that the energy barrier of the intermediate O* formation (rate-determining step) in Fe-N₂B₄ (1.83 eV) significantly decreased compared to that of Fe-N₄ (2.23 eV), demonstrating the superior of promoting ¹O₂ generation of Fe-N₂B₄. Therefore, it could be certain that B doping has successfully regulated the coordination environment and electronic structure of Fe single atom active site, changed the adsorption preference of PMS and promoted ¹O₂ production with a lower energy barrier, finally achieving ¹O₂ selective generation.

4. Conclusion

In this work, we have reported an approach to manipulate the electronic structure of the Fe single-atom site by introducing electron-depletion B atoms and constructing a six-coordination Fe-based SACs with Fe-N₂B₄ configuration. The FeN_x-B-2 catalyst (Fe-N₂B₄ configuration) exhibited excellent catalytic performance in BPA degradation with

a k_{obs} of 0.249 min^{-1} and superior $^1\text{O}_2$ generation selectivity (98.68%), which was much greater than $\text{FeN}_x\text{-600}$ (Fe-N_4 configuration, $k_{\text{obs}} = 0.191 \text{ min}^{-1}$, 64.57% of $^1\text{O}_2$ selectivity). Experimental results disclosed that the modulation of the coordination microenvironment on Fe atoms could regulate the electron density of the single-atom site, resulting in a higher valence state of Fe. Theoretical calculations confirmed that $\text{Fe-N}_2\text{B}_4$ not only downshifted the d-band center of Fe centers and facilitated the electron donation from PMS, but also significantly enhanced the selectivity for the adsorption of terminal oxygen atoms in PMS and altered the reaction pathway preference. In summary, this work demonstrated the effectiveness of precise modulation engineering by heteroatom doping on the coordination microenvironment and electronic structure of SACs for $^1\text{O}_2$ selective generation, as well as clarifying the catalytic mechanism between electronic structure and ROS generation selectivity at an atomic level. Most importantly, it afforded a facile strategy to manipulate the coordination configuration for the rational design of SACs in Fenton-like reactions toward selective elimination of contaminants in practical wastewater treatment.

CRedit authorship contribution statement

Chen Rongzhi: Formal analysis. **Zhan Xuesong:** Data curation. **Huang Wenli:** Writing – review & editing, Data curation. **Liu Dongfang:** Writing – review & editing, Supervision. **Long Yuhuan:** Writing – original draft, Software, Conceptualization. **Wu Weiran:** Validation, Software. **Cao Zhenhua:** Methodology. **Yang Peizhen:** Investigation. **Liu Wenhao:** Supervision.

Declaration of Competing Interest

The authors declare that they have no known competing financial interests or personal relationships that could have appeared to influence the work reported in this paper.

Data Availability

No data was used for the research described in the article.

Acknowledgements

The authors gratefully acknowledge the financial support from NCC Fund (NCC2020FH11) and Tianjin Natural Science Foundation (19JCQNJC08600). We would like to thank the Shiyanjia Lab (www.shiyanjia.com) for its assistance in the characterization.

Appendix A. Supporting information

Supplementary data associated with this article can be found in the online version at [doi:10.1016/j.apcatb.2023.123643](https://doi.org/10.1016/j.apcatb.2023.123643).

References

- C. Wang, H. Liu, P. Sun, J. Cai, M. Sun, H. Xie, G. Shen, A novel peroxymonosulfate activation process by single-atom iron catalyst from waste biomass for efficient singlet oxygen-mediated degradation of organic pollutants, *J. Hazard. Mater.* 453 (2023), 131333, <https://doi.org/10.1016/j.jhazmat.2023.131333>.
- K. Qian, H. Chen, W. Li, Z. Ao, Y. Wu, X. Guan, Single-Atom Fe catalyst outperforms its homogeneous counterpart for activating peroxymonosulfate to achieve effective degradation of organic contaminants, *Environ. Sci. Technol.* 55 (2021) 7034–7043, <https://doi.org/10.1021/acs.est.0c08805>.
- W. Xu, W. Xue, H. Huang, J. Wang, C. Zhong, D. Mei, Morphology controlled synthesis of $\alpha\text{-Fe}_2\text{O}_3\cdot x$ with benzimidazole-modified Fe-MOFs for enhanced photo-Fenton-like catalysis, *Appl. Catal. B Environ.* 291 (2021), 120129, <https://doi.org/10.1016/j.apcatb.2021.120129>.
- J. Wang, T. Xie, X. Liu, D. Wu, Y. Li, Z. Wang, X. Fan, F. Zhang, W. Peng, Enhanced redox cycle of $\text{Fe}^{3+}/\text{Fe}^{2+}$ on Fe@NC by boron: Fast electron transfer and long-term stability for Fenton-like reaction, *J. Hazard. Mater.* 445 (2023), 130605, <https://doi.org/10.1016/j.jhazmat.2022.130605>.
- B. Zhang, X. Li, P.A. Bingham, K. Akiyama, S. Kubuki, Carbon matrix with atomic dispersion of binary cobalt/iron-N sites as efficient peroxymonosulfate activator for organic pollutant oxidation, *Chem. Eng. J.* 451 (2023), 138574, <https://doi.org/10.1016/j.cej.2022.138574>.
- S. Wu, Z. Yang, Z. Zhou, X. Li, Y. Lin, J.J. Cheng, C. Yang, Catalytic activity and reaction mechanisms of single-atom metals anchored on nitrogen-doped carbons for peroxymonosulfate activation, *J. Hazard. Mater.* 459 (2023), 132133, <https://doi.org/10.1016/j.jhazmat.2023.132133>.
- B. Zhang, X. Li, K. Akiyama, P.A. Bingham, S. Kubuki, Elucidating the mechanistic origin of a spin state-dependent $\text{FeN}_x\text{-C}$ catalyst toward organic contaminant oxidation via peroxymonosulfate activation, *Environ. Sci. Technol.* 56 (2022) 1321–1330, <https://doi.org/10.1021/acs.est.1c05980>.
- Z. Wang, E. Almatrafi, H. Wang, H. Qin, W. Wang, L. Du, S. Chen, G. Zeng, P. Xu, Cobalt single atoms anchored on oxygen-doped tubular carbon nitride for efficient peroxymonosulfate activation: simultaneous coordination structure and morphology modulation, *Angew. Chem. Int. Ed.* 61 (2022), e202202338, <https://doi.org/10.1002/anie.202202338>.
- Y. He, H. Qin, Z. Wang, H. Wang, Y. Zhu, C. Zhou, Y. Zeng, Y. Li, P. Xu, G. Zeng, Fe-Mn oxycarbide anchored on N-doped carbon for enhanced Fenton-like catalysis: Importance of high-valent metal-oxo species and singlet oxygen, *Appl. Catal. B Environ.* 340 (2024), 123204, <https://doi.org/10.1016/j.apcatb.2023.123204>.
- J. Sun, L. Wang, Y. Wang, W. Lv, Y. Yao, Activation of peroxymonosulfate by MgCoAl layered double hydroxide: Potential enhancement effects of catalyst morphology and coexisting anions, *Chemosphere* 286 (2022), 131640, <https://doi.org/10.1016/j.chemosphere.2021.131640>.
- Q. Zhou, C. Song, P. Wang, Z. Zhao, Y. Li, S. Zhan, Generating dual-active species by triple-atom sites through peroxymonosulfate activation for treating micropollutants in complex water, *Proc. Natl. Acad. Sci. U. S. A.* 120 (2023), e2300085120, <https://doi.org/10.1073/pnas.2300085120>.
- J. Xie, X. Luo, L. Chen, X. Gong, L. Zhang, J. Tian, ZIF-8 derived boron, nitrogen co-doped porous carbon as metal-free peroxymonosulfate activator for tetracycline hydrochloride degradation: performance, mechanism and biotoxicity, *Chem. Eng. J.* 440 (2022), 135760, <https://doi.org/10.1016/j.cej.2022.135760>.
- Y. Yao, C. Wang, X. Yan, H. Zhang, C. Xiao, J. Qi, Z. Zhu, Y. Zhou, X. Sun, X. Duan, J. Li, Rational regulation of Co-N-C coordination for high-efficiency generation of $^1\text{O}_2$ toward Nearly 100% selective degradation of organic pollutants, *Environ. Sci. Technol.* 56 (2022) 8833–8843, <https://doi.org/10.1021/acs.est.2c00706>.
- Z. Wang, Y. Wang, W. Wang, D. Wu, Q. Wu, H. Hu, Highly selective production of singlet oxygen by manipulating the spin state of single-atom Co-N moieties and electron localization, *Appl. Catal. B Environ.* 324 (2023), 122248, <https://doi.org/10.1016/j.apcatb.2022.122248>.
- X. Wang, Z. Xiong, H. Shi, Z. Wu, B. Huang, H. Zhang, P. Zhou, Z. Pan, W. Liu, B. Lai, Switching the reaction mechanisms and pollutant degradation routes through active center size-dependent Fenton-like catalysis, *Appl. Catal. B Environ.* 329 (2023), 122569, <https://doi.org/10.1016/j.apcatb.2023.122569>.
- J. Miao, Y. Zhu, J. Lang, J. Zhang, S. Cheng, B. Zhou, L. Zhang, P.J.J. Alvarez, M. Long, Spin-state-dependent peroxymonosulfate activation of single-atom M-N moieties via a radical-free pathway, *ACS Catal.* 11 (2021) 9569–9577, <https://doi.org/10.1021/acscatal.1c02031>.
- X. Mi, P. Wang, S. Xu, L. Su, H. Zhong, H. Wang, Y. Li, S. Zhan, Almost 100% peroxymonosulfate conversion to singlet oxygen on single-atom CoN_{2+2} sites, *Angew. Chem. Int. Ed.* 60 (2021) 4588–4593, <https://doi.org/10.1002/anie.202014472>.
- M. Yang, K. Wu, S. Sun, J. Duan, X. Liu, J. Cui, S. Liang, Y. Ren, Unprecedented relay catalysis of curved $\text{Fe}_1\text{-N}_4$ single-atom site for remarkably efficient $^1\text{O}_2$ generation, *ACS Catal.* 13 (2023) 681–691, <https://doi.org/10.1021/acscatal.2c05409>.
- B. Huang, X. Ren, J. Zhao, Z. Wu, X. Wang, X. Song, X. Li, B. Liu, Z. Xiong, B. Lai, Modulating electronic structure engineering of atomically dispersed cobalt catalyst in Fenton-like reaction for efficient degradation of organic pollutants, *Environ. Sci. Technol.* 57 (2023) 14071–14081, <https://doi.org/10.1021/acs.est.3c04712>.
- Z. Zhao, H. Tan, P. Zhang, X. Liang, T. Li, Y. Gao, C. Hu, Turning the inert element zinc into an active single-atom catalyst for efficient Fenton-like chemistry, *Angew. Chem. Int. Ed.* 62 (2023), e202219178, <https://doi.org/10.1002/anie.202219178>.
- J. Wang, W. Qiu, G. Li, J. Liu, D. Luo, Y. Zhang, Y. Zhao, G. Zhou, L. Shui, X. Wang, Z. Chen, Coordinatively deficient single-atom Fe-N-C electrocatalyst with optimized electronic structure for high-performance lithium-sulfur batteries, *Energy Storage Mater.* 46 (2022) 269–277, <https://doi.org/10.1016/j.ensm.2021.12.040>.
- X. Liang, D. Wang, Z. Zhao, T. Li, Y. Gao, C. Hu, Coordination number dependent catalytic activity of single-atom cobalt catalysts for Fenton-like reaction, *Adv. Funct. Mater.* 32 (2022), 2203001, <https://doi.org/10.1002/adfm.202203001>.
- C. Zhu, Y. Nie, F. Cun, Y. Wang, Z. Tian, F. Liu, Two-step pyrolysis to anchor ultrahigh-density single-atom FeN_5 sites on carbon nitride for efficient Fenton-like catalysis near 0°C , *Appl. Catal. B Environ.* 319 (2022), 121900, <https://doi.org/10.1016/j.apcatb.2022.121900>.
- Z. Wang, W. Wang, J. Wang, Y. Yuan, Q. Wu, H. Hu, High-valent iron-oxo species mediated cyclic oxidation through single-atom Fe-N_6 sites with high peroxymonosulfate utilization rate, *Appl. Catal. B Environ.* 305 (2022), 121049, <https://doi.org/10.1016/j.apcatb.2021.121049>.
- C. Wang, X. Wang, H. Wang, L. Zhang, Y. Wang, C.-L. Dong, Y.-C. Huang, P. Guo, R. Cai, S.J. Haigh, X. Yang, Y. Sun, D. Yang, Low-coordinated Co-N_3 sites induce peroxymonosulfate activation for norfloxacin degradation via high-valent cobalt-oxo species and electron transfer, *J. Hazard. Mater.* 455 (2023), 131622, <https://doi.org/10.1016/j.jhazmat.2023.131622>.
- Y. Zou, J. Hu, B. Li, L. Lin, Y. Li, F. Liu, X. Li, Tailoring the coordination environment of cobalt in a single-atom catalyst through phosphorus doping for enhanced activation of peroxymonosulfate and thus efficient degradation of

- sulfadiazine, *Appl. Catal. B Environ.* 312 (2022), 121408, <https://doi.org/10.1016/j.apcatb.2022.121408>.
- [27] L. Jiao, Y. Kang, Y. Chen, N. Wu, Y. Wu, W. Xu, X. Wei, H. Wang, W. Gu, L. Zheng, W. Song, C. Zhu, Unsymmetrically coordinated single Fe-N₃S₁ sites mimic the function of peroxidase, *Nano Today* 40 (2021), 101261, <https://doi.org/10.1016/j.nantod.2021.101261>.
- [28] P. Yang, Z. Cao, Y. Long, D. Liu, W. Huang, S. Zhan, M. Li, Regulating the local electronic structure of copper single atoms with unsaturated B₃O₃-Coordination for Selective ¹O₂ generation, *ACS Catal.* 13 (2023) 12414–12424, <https://doi.org/10.1021/acscatal.3c03303>.
- [29] J. Song, N. Hou, X. Liu, M. Antonietti, P. Zhang, R. Ding, L. Song, Y. Wang, Y. Mu, Asymmetrically coordinated CoB₃N₃ moieties for selective generation of high-valence Co-Oxo species via coupled electron-proton transfer in Fenton-like reactions, *Adv. Mater.* 35 (2023), 2209552, <https://doi.org/10.1002/adma.202209552>.
- [30] X. Chen, X. Duan, W.-D. Oh, P.-H. Zhang, C.-T. Guan, Y.-A. Zhu, T.-T. Lim, Insights into nitrogen and boron-co-doped graphene toward high-performance peroxymonosulfate activation: maneuverable N-B bonding configurations and oxidation pathways, *Appl. Catal. B Environ.* 253 (2019) 419–432, <https://doi.org/10.1016/j.apcatb.2019.04.018>.
- [31] Y. Dai, H. Li, C. Wang, W. Xue, M. Zhang, D. Zhao, J. Xue, J. Li, L. Luo, C. Liu, X. Li, P. Cui, Q. Jiang, T. Zheng, S. Gu, Y. Zhang, J. Xiao, C. Xia, J. Zeng, Manipulating local coordination of copper single atom catalyst enables efficient CO₂-to-CH₄ conversion, *Nat. Commun.* 14 (2023), 3382, <https://doi.org/10.1038/s41467-023-39048-6>.
- [32] S. Liu, M. Jin, J. Sun, Y. Qin, S. Gao, Y. Chen, S. Zhang, J. Luo, X. Liu, Coordination environment engineering to boost electrocatalytic CO₂ reduction performance by introducing boron into single-Fe-atomic catalyst, *Chem. Eng. J.* 437 (2022), 135294, <https://doi.org/10.1016/j.cej.2022.135294>.
- [33] Y. Wang, H. Li, F. Peng, F. Gao, Boron induced electron-rich single iron sites for boosted N₂ electroreduction reaction, *Chem. Eng. J.* 445 (2022), 136692, <https://doi.org/10.1016/j.cej.2022.136692>.
- [34] Y. Gao, T. Wu, C. Yang, C. Ma, Z. Zhao, Z. Wu, S. Cao, W. Geng, Y. Wang, Y. Yao, Y. Zhang, C. Cheng, Activity trends and mechanisms in peroxymonosulfate-assisted catalytic production of singlet oxygen over atomic metal-N-C catalysts, *Angew. Chem. Int. Ed.* 60 (2021) 22513–22521, <https://doi.org/10.1002/anie.202109530>.
- [35] L.-S. Zhang, X.-H. Jiang, Z.-A. Zhong, L. Tian, Q. Sun, Y.-T. Cui, X. Lu, J.-P. Zou, S.-L. Luo, Carbon nitride supported high-loading Fe single-atom catalyst for activation of peroxymonosulfate to generate ¹O₂ with 100% selectivity, *Angew. Chem. Int. Ed.* 60 (2021) 21751–21755, <https://doi.org/10.1002/anie.202109488>.
- [36] X. Zhao, X. Li, Z. Zhu, W. Hu, H. Zhang, J. Xu, X. Hu, Y. Zhou, M. Xu, H. Zhang, G. Hu, Single-atom Co embedded in BCN matrix to achieve 100% conversion of peroxymonosulfate into singlet oxygen, *Appl. Catal. B Environ.* 300 (2022), 120759, <https://doi.org/10.1016/j.apcatb.2021.120759>.
- [37] D. Yu, L. Li, M. Wu, J.C. Crittenden, Enhanced photocatalytic ozonation of organic pollutants using an iron-based metal-organic framework, *Appl. Catal. B Environ.* 251 (2019) 66–75, <https://doi.org/10.1016/j.apcatb.2019.03.050>.
- [38] J. VandeVondele, M. Krack, F. Mohamed, M. Parrinello, T. Chassaing, J. Hutter, Quickstep: fast and accurate density functional calculations using a mixed Gaussian and plane waves approach, *Comput. Phys. Commun.* 167 (2005) 103–128, <https://doi.org/10.1016/j.cpc.2004.12.014>.
- [39] S. Goedecker, M. Teter, J. Hutter, Separable dual-space Gaussian pseudopotentials, *Phys. Rev. B* 54 (1996) 1703–1710, <https://doi.org/10.1103/PhysRevB.54.1703>.
- [40] J. VandeVondele, J. Hutter, Gaussian basis sets for accurate calculations on molecular systems in gas and condensed phases, *J. Chem. Phys.* 127 (2007), 114105, <https://doi.org/10.1063/1.2770708>.
- [41] J.P. Perdew, K. Burke, M. Ernzerhof, Generalized gradient approximation made simple, *Phys. Rev. Lett.* 77 (1996) 3865–3868, <https://doi.org/10.1103/PhysRevLett.77.3865>.
- [42] S. Grimme, J. Antony, S. Ehrlich, H. Krieg, A consistent and accurate ab initio parametrization of density functional dispersion correction (DFT-D) for the 94 elements H-Pu, *J. Chem. Phys.* 132 (2010), 154104, <https://doi.org/10.1063/1.3382344>.
- [43] T. Lu, F. Chen, Multiwfn: a multifunctional wavefunction analyzer, *J. Comput. Chem.* 33 (2012) 580–592, <https://doi.org/10.1002/jcc.22885>.
- [44] B. Liu, W. Guo, H. Wang, Q. Si, Q. Zhao, H. Luo, N. Ren, B-doped graphitic porous biochar with enhanced surface affinity and electron transfer for efficient peroxodisulfate activation, *Chem. Eng. J.* 396 (2020), 125119, <https://doi.org/10.1016/j.cej.2020.125119>.
- [45] J. Dou, J. Cheng, Z. Lu, Z. Tian, J. Xu, Y. He, Biochar co-doped with nitrogen and boron switching the free radical based peroxodisulfate activation into the electron-transfer dominated nonradical process, *Appl. Catal. B Environ.* 301 (2022), 120832, <https://doi.org/10.1016/j.apcatb.2021.120832>.
- [46] H. Fu, J. Wei, G. Chen, M. Xu, J. Liu, J. Zhang, K. Li, Q. Xu, Y. Zou, W. Zhang, S. Xi, X. Chen, S. Li, L. Ling, Axial coordination tuning Fe single-atom catalysts for boosting H₂O₂ activation, *Appl. Catal. B Environ.* 321 (2023), 122012, <https://doi.org/10.1016/j.apcatb.2022.122012>.
- [47] C. Liang, H. Sun, C. Ling, X. Liu, M. Li, X. Zhang, F. Guo, X. Zhang, Y. Shi, S. Cao, H. He, Z. Ai, L. Zhang, Pyrolysis temperature-switchable Fe-N sites in pharmaceutical sludge biochar toward peroxymonosulfate activation for efficient pollutants degradation, *Water Res.* 228 (2023), 119328, <https://doi.org/10.1016/j.watres.2022.119328>.
- [48] Z. Wang, E. Almatrafi, H. Wang, H. Qin, W. Wang, L. Du, S. Chen, G. Zeng, P. Xu, Cobalt single atoms anchored on oxygen-doped tubular carbon nitride for efficient peroxymonosulfate activation: simultaneous coordination structure and morphology modulation, *Angew. Chem. Int. Ed.* 61 (2022), e202202338, <https://doi.org/10.1002/anie.202202338>.
- [49] X. Chen, X. Duan, W.-D. Oh, P.-H. Zhang, C.-T. Guan, Y.-A. Zhu, T.-T. Lim, Insights into nitrogen and boron-co-doped graphene toward high-performance peroxymonosulfate activation: maneuverable N-B bonding configurations and oxidation pathways, *Appl. Catal. B Environ.* 253 (2019) 419–432, <https://doi.org/10.1016/j.apcatb.2019.04.018>.
- [50] C. Zhu, Y. Nie, S. Zhao, Z. Fan, F. Liu, A. Li, Constructing surface micro-electric fields on hollow single-atom cobalt catalyst for ultrafast and anti-interference advanced oxidation, *Appl. Catal. B Environ.* 305 (2022), 121057, <https://doi.org/10.1016/j.apcatb.2021.121057>.
- [51] J. Cui, L. Li, S. Shao, J. Gao, K. Wang, Z. Yang, S. Zeng, C. Diao, Y. Zhao, C. Hu, Regulating the metal-support interaction: double jump to reach the efficiency apex of the Fe-N₃-catalyzed Fenton-like reaction, *ACS Catal.* 12 (2022) 14954–14963, <https://doi.org/10.1021/acscatal.2c04287>.
- [52] B. Huang, Z. Wu, X. Wang, X. Song, H. Zhou, H. Zhang, P. Zhou, W. Liu, Z. Xiong, B. Lai, Coupled surface-confinement effect and pore engineering in a Single-Fe-Atom catalyst for ultrafast Fenton-like reaction with high-valent iron-oxo complex oxidation, *Environ. Sci. Technol.* 57 (2023) 15667–15679, <https://doi.org/10.1021/acs.est.3c05509>.
- [53] J. Wang, H. Li, S. Liu, Y. Hu, J. Zhang, M. Xia, Y. Hou, J. Tse, J. Zhang, Y. Zhao, Turning on Zn 4s Electrons in a N₂-Zn-B₃ Configuration to Stimulate Remarkable ORR Performance, *Angew. Chem. Int. Ed.* 60 (2021) 181–185, <https://doi.org/10.1002/anie.202009991>.
- [54] L. Zhang, Y. Sun, R. Ge, W. Zhou, Z. Ao, J. Wang, Mechanical insight into direct singlet oxygen generation pathway: Pivotal role of FeN₄ sites and selective organic contaminants removal, *Appl. Catal. B Environ.* 339 (2023), 123130, <https://doi.org/10.1016/j.apcatb.2023.123130>.
- [55] L.J. Peng, X.G. Duan, Y.N. Shang, B.Y. Gao, X. Xu, Engineered carbon supported single iron atom sites and iron clusters from Fe-rich Enteromorpha for Fenton-like reactions via nonradical pathways, *Appl. Catal. B Environ.* 287 (2021), 119963, <https://doi.org/10.1016/j.apcatb.2021.119963>.
- [56] Z. Wu, B. Huang, X. Wang, C.-S. He, Y. Liu, Y. Du, W. Liu, Z. Xiong, B. Lai, Facilely tuning the first-shell coordination microenvironment in iron single-atom for Fenton-like chemistry toward highly efficient wastewater purification, *Environ. Sci. Technol.* 57 (2023) 14046–14057, <https://doi.org/10.1021/acs.est.3c04343>.
- [57] K. Yin, Y. Shang, D. Chen, B. Gao, Q. Yue, X. Xu, Redox potentials of pollutants determining the dominate oxidation pathways in manganese single-atom catalyst (Mn-SAC)/peroxymonosulfate system: selective catalytic mechanisms for versatile pollutants, *Appl. Catal. B Environ.* 338 (2023), 123029, <https://doi.org/10.1016/j.apcatb.2023.123029>.
- [58] J. Song, N. Hou, X. Liu, M. Antonietti, Y. Wang, Y. Mu, Unsaturated single-atom CoN₃ sites for improved Fenton-like reaction towards high-valent metal species, *Appl. Catal. B Environ.* 325 (2023), 122368, <https://doi.org/10.1016/j.apcatb.2023.122368>.
- [59] C. Cheng, W. Ren, F. Miao, X. Chen, X. Chen, H. Zhang, Generation of Fe^{IV}=O and its Contribution to Fenton-Like Reactions on a Single-Atom Iron-N-C catalyst, *Angew. Chem. Int. Ed.* 62 (2023), e202218510, <https://doi.org/10.1002/anie.202218510>.
- [60] S. Wang, J. Wang, Single atom cobalt catalyst derived from co-pyrolysis of vitamin B12 and graphitic carbon nitride for PMS activation to degrade emerging pollutants, *Appl. Catal. B Environ.* 321 (2023), 122051, <https://doi.org/10.1016/j.apcatb.2022.122051>.
- [61] Y. Zhang, X. Chen, C. Liang, L. Yin, Y. Yang, Reconstructing the coordination environment of single atomic Fe-catalysts for boosting the Fenton-like degradation activities, *Appl. Catal. B Environ.* 315 (2022), 121536, <https://doi.org/10.1016/j.apcatb.2022.121536>.
- [62] G. Yang, J. Zhu, P. Yuan, Y. Hu, G. Qu, B.-A. Lu, X. Xue, H. Yin, W. Cheng, J. Cheng, W. Xu, J. Li, J. Hu, S. Mu, J.-N. Zhang, Regulating Fe-spin state by atomically dispersed Mn-N in Fe-N-C catalysts with high oxygen reduction activity, *Nat. Commun.* 12 (2021), 1734, <https://doi.org/10.1038/s41467-021-21919-5>.
- [63] X. Liang, D. Wang, Z. Zhao, T. Li, Z. Chen, Y. Gao, C. Hu, Engineering the low-coordinated single cobalt atom to boost persulfate activation for enhanced organic pollutant oxidation, *Appl. Catal. B Environ.* 303 (2022), 120877, <https://doi.org/10.1016/j.apcatb.2021.120877>.
- [64] X. Li, X. Wen, J. Lang, Y. Wei, J. Miao, X. Zhang, B. Zhou, M. Long, P.J.J. Alvarez, L. Zhang, CoN₁O₂ single-atom catalyst for efficient peroxymonosulfate activation and selective Cobalt(IV)=O generation, *Angew. Chem. Int. Ed.* 62 (2023), e202303267, <https://doi.org/10.1002/anie.202303267>.
- [65] F. Chen, L.-L. Liu, J.-H. Wu, X.-H. Rui, J.-J. Chen, Y. Yu, Single-atom iron anchored tubular g-C₃N₄ catalysts for ultrafast Fenton-like reaction: roles of high-valency Iron-Oxo species and organic radicals, *Adv. Mater.* 34 (2022), 2202891, <https://doi.org/10.1002/adma.202202891>.
- [66] P. Yang, Y. Long, W. Huang, D. Liu, Single-atom copper embedded in two-dimensional MXene toward peroxymonosulfate activation to generate singlet oxygen with nearly 100% selectivity for enhanced Fenton-like reactions, *Appl. Catal. B Environ.* 324 (2023), 122245, <https://doi.org/10.1016/j.apcatb.2022.122245>.
- [67] Q.-Y. Wu, Z.-W. Yang, Z.-W. Wang, W.-L. Wang, Oxygen doping of cobalt-single-atom coordination enhances peroxymonosulfate activation and high-valent cobalt-oxo species formation, *Proc. Natl. Acad. Sci. U. S. A.* 120 (2023), e2219923120, <https://doi.org/10.1073/pnas.2219923120>.
- [68] Y. Gao, Y. Zhu, T. Li, Z. Chen, Q. Jiang, Z. Zhao, X. Liang, C. Hu, Unraveling the high-activity origin of single-atom iron catalysts for organic pollutant oxidation via

- peroxymonosulfate activation, *Environ. Sci. Technol.* 55 (2021) 8318–8328, <https://doi.org/10.1021/acs.est.1c01131>.
- [69] H. Zeng, S. Liu, B. Chai, D. Cao, Y. Wang, X. Zhao, Enhanced photoelectrocatalytic decomplexation of Cu-EDTA and Cu recovery by persulfate activated by UV and cathodic reduction, *Environ. Sci. Technol.* 50 (2016) 6459–6466, <https://doi.org/10.1021/acs.est.6b00632>.
- [70] F. Xu, C. Lai, M. Zhang, B. Li, L. Li, S. Liu, D. Ma, X. Zhou, H. Yan, X. Huo, B. Wang, H. Yi, L. Qin, L. Tang, High-loaded single-atom Cu-N₃ sites catalyze hydrogen peroxide decomposition to selectively induce singlet oxygen production for wastewater purification, *Appl. Catal. B Environ.* 339 (2023), 123075, <https://doi.org/10.1016/j.apcatb.2023.123075>.